

31 **Abstract.**

32

33 This study aims to better understand and quantify the uncertainties in microwave snow
34 emission models using the Dense Media Radiative Theory-Multilayer model (DMRT-
35 ML) with in-situ measurements of snow properties. We use surface-based radiometric
36 measurements at 10.67, 19 and 37 GHz in boreal forest and subarctic environments, and a
37 new in situ dataset of measurements of snow properties (profiles of density, snow grain
38 size and temperature, soil characterization and ice lens detection) acquired in the James
39 Bay and Umiujaq regions of Northern Québec, Canada. A snow excavation experiment --
40 where snow was removed from the ground to measure the microwave emission of bare
41 frozen ground -- shows that small-scale spatial variability (less than 1 km) in the emission
42 of frozen soil is small. Hence, in our case of boreal organic soil, variability in the
43 emission of frozen soil has a small effect on snow-covered brightness temperature (T_B).
44 Grain size and density measurement errors can explain the errors at 37 GHz, while the
45 sensitivity of T_B at 19 GHz to snow increases during the winter because of the snow grain
46 growth that leads to scattering. Furthermore, the inclusion of observed ice lenses in
47 DMRT-ML leads to significant improvements in the simulations at horizontal
48 polarization (H-pol) for the three frequencies (up to 20 K of root mean square error).
49 However, representation of the spatial variability of T_B remains poor at 10.67 and 19 GHz
50 at H-pol given the spatial variability of ice lens characteristics and the difficulty in
51 simulating snowpack stratigraphy related to the snow crust. The results also show that, in
52 our study with the given forest characteristics, forest emission reflected by the surface
53 can increase the T_B up to 40 K. The forest contribution varies with vegetation
54 characteristics and a relationship between the downwelling contribution of vegetation
55 and the proportion of pixels occupied by vegetation (trees) in fisheye pictures was found.
56 We perform a comprehensive analysis of the components that contribute to the
57 snow-covered microwave signal, which will help to develop DMRT-ML and to
58 improve the required field measurements. The analysis shows that a better consideration
59 of ice lenses and snow crusts is essential to improve T_B simulations in boreal forest
60 and subarctic environments.

61

62 Keywords: DMRT-ML, snow, vegetation, ice lenses, soil emissivity, microwave

63

64 **1. Introduction**

65

66 Seasonal snow cover plays an important role in the surface energy balance (Armstrong
67 and Brun, 2008). Snow, with its low thermal conductivity, has an insulating effect on
68 soils, which can greatly influence vegetation (Liston et al., 2002) and the development of
69 active layers in permafrost (Gouttevin et al., 2012; Shurr et al., 2013). Snow water
70 equivalent (SWE) is also a key variable in the high latitude water cycle (Déry et al.,
71 2009) and is important for dam management and hydroelectricity production (Roy et al.,
72 2010). Conventional in situ observations, such as from meteorological stations, are often
73 inadequate to monitor seasonal snow evolution given the sparse distribution of stations in
74 northern regions. Furthermore, point measurements are subject to local scale variability
75 and may not represent the prevailing regional conditions. For these reasons, monitoring
76 SWE from satellite passive microwave (PMW) observations has been the subject of

77 numerous studies for nearly three decades (e.g., Chang et al. 1987; Goodison et al., 1986;
78 Derksen, 2008). The PMW are sensitive to SWE, but also have the advantage of
79 providing observations at a synoptic scale in any weather conditions: images are available
80 at least twice a day for the northern regions. However, estimation of SWE is not
81 straightforward and existing empirical algorithms based on linear relationships between
82 SWE and spectral T_B are often inaccurate due to seasonal snow grain metamorphism
83 (Rosenfeld and Grody, 2000). Vegetation contributions are also an important factor with
84 large interannual variability (Roy et al., 2015), which is not captured by these algorithms.
85 Hence, radiative transfer models (RTM) including microwave snow emission models
86 (MSEM) can be used to take into account the different contributions to the microwave
87 signal and the interannual variability of critical geophysical parameters. The GlobSnow2
88 SWE retrieval algorithm (Takala et al., 2011) uses an assimilation scheme combining
89 PMW observations constrained with kriged measurements of snow depth from
90 meteorological stations. This method, however, has some limitations in remote areas
91 where snow measurements are sparse, thus highlighting the need to improve MSEM
92 performance in such a way that SWE retrievals can be achieved without in situ
93 observations (Larue et al., 2015).

94
95 At the satellite scale, PMW observations generally have a coarse spatial resolution (more
96 than 10 km x 10 km). Nevertheless, spatial heterogeneity within PMW pixels becomes a
97 limitation for the development and validation of MSEM because contributions from
98 snow, vegetation and lakes are difficult to decouple. Therefore, surface-based
99 radiometers (SBR) are used to better understand and isolate the contribution of snow-
100 covered surfaces. However, independently of MSEM used and seasonal snow type, the
101 comparison between simulated T_B and SBR observations leads to errors in the order of 10
102 K (Roy et al., 2013; Montpetit et al., 2013; Derksen et al., 2012; Kontu and Pulliainen,
103 2010; Lemmetyinen et al., 2010; Lemmetyinen et al., 2015; Durand et al., 2008). From
104 SBR measurements, these errors can be explained by 1) MSEM physical simplification
105 (Tedesco and Kim, 2006) and 2) small scale variability and uncertainty in measurements
106 of geophysical parameters.

107
108 Hence, this paper aims to better quantify the relative importance of different geophysical
109 parameters and small-scale spatial variability when simulating microwave T_B with the
110 Dense Media Radiative Theory-Multilayer model (DMRT-ML; Picard et al. 2013). The
111 study is based on a new and unique database including SBR measurements at three
112 microwave frequencies (37, 19 and 10.67 GHz) in boreal and subarctic environments.
113 The study assesses a wide range of contributions that could lead to uncertainties in
114 ground-based microwave snow emission modeling: snow grains, snow density, soil
115 roughness, ice lenses (IL) and vegetation. More specifically, the objectives of the study
116 are:

117
118 1. Validate the snow emission modeling, including recent improvements accounting for
119 ice lenses (Montpetit et al., 2013) and snow density in the 367-550 kg m⁻³ range
120 (Dierking et al., 2012).

122 2. Evaluate the different contributions to modeling uncertainty (snow grains, snow
123 density, ice lenses, soil and vegetation measurements).

124

125 3. Quantify the sensitivity of simulated T_B to the measurement accuracy.

126

127 2. Method

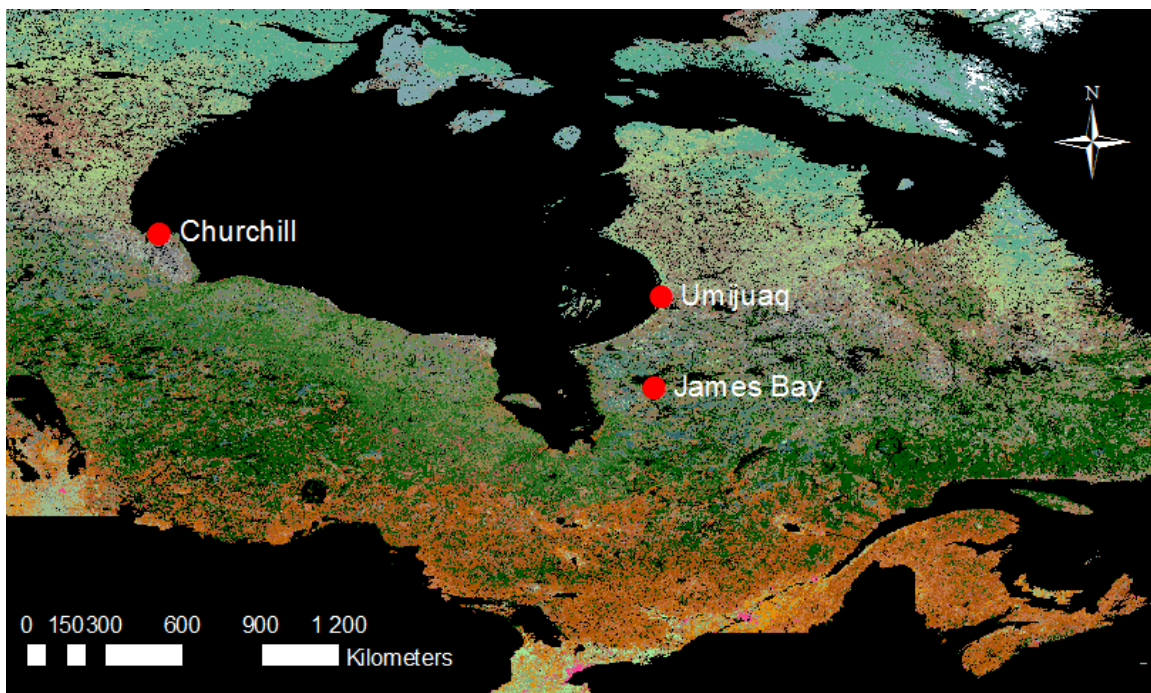
128

129 2.1 Sites and Data

130

131 Surface-based radiometer observations were acquired during the 2010 field campaign at
132 the Churchill Northern Studies Center (Northern Manitoba) (see Roy et al., 2013 for a
133 detailed description of the field campaign) and during four subsequent field campaigns in
134 Northern Québec, Canada: three in James Bay ($53^{\circ}26'N$; $76^{\circ}46'W$, 186 m a.s.l) in winter
135 2013 and one campaign in Umiujaq ($56^{\circ}33'N$, $76^{\circ}30'W$, 74 m a.s.l) in winter 2014 (Fig.
136 1). All these campaign allow covering a wide range of environmental conditions from
137 dense boreal forest to open tundra for a total of 51 snowpits (excluding the Churchill
138 snowpits).

139



140

141 Fig. 1. Location of field campaigns. Background: Land Cover of Canada (Latifovic et al.,
142 2004)

143

144 T_B measurements were acquired at 37, 19 and 10.67 GHz in both vertical (V-pol) and
145 horizontal (H-pol) polarizations at a height of approximately 1.5 m above the ground and
146 at an angle of 55° with the PR-series Surface-Based Radiometers from Radiometrics
147 Corporation (Langlois, 2015) (hereinafter, the 10.67 GHz SBR is noted 11 GHz for
148 simplicity). With a beam width of 6° for 37 and 19 GHz SBR, the footprint of the
149 measurements at the snow surface was approximately 0.6 m x 0.6 m. The 11 GHz beam
150 width is 8° with a footprint of about 0.8 x 0.8 m. In the worst case, the measurement error

151 for the calibration target was estimated at 2 K. The radiometers were calibrated before
152 and after each field campaign using ambient (black body) and cold (liquid nitrogen)
153 targets.

154

155 Within the footprint of every SBR observation, profiles of snow temperature, snow
156 density (ρ_{snow} in kg m^{-3}) and specific surface area (SSA in $\text{m}^2 \text{kg}^{-1}$) were taken at a
157 vertical resolution between 3 and 5 cm. Visual stratigraphy assessment of the main snow
158 layers/features, including ice lenses, was conducted. The density was measured using a
159 185-cm^3 density cutter, and samples were weighed with a 100-g Pesola light series scale
160 with an accuracy of 0.5 g. The snow temperature and soil temperature were measured
161 with a Traceable 2000 digital temperature probe (± 0.1 °C). The SSA was measured with
162 the shortwave InfraRed Integrating Sphere (IRIS) system (Montpetit et al., 2012) at the
163 James Bay site and using the Dual Frequency Integrating Sphere for Snow SSA
164 measurement (DUFISSS: Gallet et al., 2009) in Umiujaq. Both instruments exploit the
165 relationship between the SWIR snow reflectance and the SSA (Kokhanovsky and Zege,
166 2004) based on the principle described in Gallet et al. (2009). From SSA measurements,
167 the optical radius of the snow grain (R_{opt}) was calculated by:

168

$$169 \quad R_{\text{opt}} = \frac{3}{\rho_{\text{ice}} \text{SSA}} \quad (1)$$

170

171 where ρ_{ice} is the ice density = 917 kg m^{-3} . The SSA is one of the most robust and
172 objective approaches to measure a parameter related to the size of snow grains in the
173 field. The error for SSA measurements was estimated to be 12% (Gallet et al., 2009).

174

175 **2.1.1 James Bay, Québec, Canada**

176

177 Three intensive measurement periods were conducted during the 2013 winter season in
178 the James Bay area, Québec, in January (8th to 12th: JB_{Jan}), February (12th to 17th: JB_{Feb})
179 and March (19th to 23th: JB_{Mar}) (Tables 1, 2 and 3). The sites were in a typical boreal
180 forest environment, but most of the measurements were conducted in clearings with
181 minimal influence of the environment (topography, vegetation) on the measured T_B .
182 However, 15 measurements, spanning across the three campaigns, were conducted in
183 forested areas and were treated separately to specifically investigate the contribution of
184 vegetation on the ground-based measurements (Table 4). Several snow excavation
185 experiments (denoted SEex) were also conducted where snow was removed to measure
186 frozen ground emission. During SEex, large snowpits were dug (about 3 m x 3 m wide)
187 and the snow walls removed to eliminate snow wall emission reflected on the ground. At
188 all sites, the soil (described below) was frozen at least to a depth of 10 cm.

189

190 During the JB_{Jan} campaign, 16 open area sites were measured where the mean ρ_{snow}
191 (weighted by snow layers thickness excluding ice lenses) of all snowpits was 218.3 kg m^{-3}
192 and the mean R_{opt} (weighted by snow layers thickness excluding ice lenses) was 0.17
193 mm (Table 1). Snowpits JB_{Jan}-1 to JB_{Jan}-5 were located in forest clearings where the soil
194 composition mainly consisted of organic matter. On January 9th, a transect of 11 snowpits
195 (JB_{Jan}-6.1 to JB_{Jan}-6.11, each separated by 3 m) was conducted in an old gravel pit

196 (mostly mineral soil). Five SEex were also conducted in the 30 m transect. One to two ice
 197 lenses of about 0.5 to 1 cm were observed in all snowpits, buried at depths of 10 and 30
 198 cm.

199

200 **Table 1.** Average snow property values with standard deviation (in parentheses) at James
 201 Bay (JB) sites in January. Values are provided for snow depth (SD m); mean snowpack
 202 temperature (T_{snow}); bulk density (ρ_{snow}); mean optical radius (R_{opt}); soil/snow temperature
 203 (T_{soil}); number of observed ice lenses (IL); and ‘bridging’ (B) indicates the presence of a
 204 snow layer with a density within the bridging ice fraction limits (see Sect. 2.2.2).

SP	Type	SD (cm)	T_{snow} (K)	ρ_{snow} (kg m ⁻³)	R_{opt} (mm)	T_{soil} (K)	IL	B	Date
JB _{an} -1	Forest clearing Organic soil	37	259.9 (4.8)	220.7 (37.4)	0.19 (0.09)	272.3	1		07-01-2013
JB _{an} -2		43	265.3 (3.4)	196.3 (40.4)	0.15 (0.07)	272.0	1		08-01-2013
JB _{an} -3		48	264.8 (4.2)	241.1 (37.2)	0.20 (0.10)	272.6	1		08-01-2013
JB _{an} -4		48	264.9 (3.6)	212.8 (48.5)	0.17 (0.09)	272.3	1		08-01-2013
JB _{an} -5		62	267.5 (1.8)	220.8 (45.9)	0.15 (0.08)	272.4	1		11-01-2013
JB _{an} -6.1	Old gravel pit Mineral soil JB _{an} -transect	51	266.8 (2.4)	223.4 (39.6)	0.17 (0.08)	271.5	1		09-01-2013
JB _{an} -6.2		52	267.4 (2.4)	240.1 (42.5)	0.18 (0.08)	271.5	1		09-01-2013
JB _{an} -6.3		43	266.5 (1.4)	212.8 (34.9)	0.17 (0.08)	271.3	1		09-01-2013
JB _{an} -6.4		45	268.0 (2.3)	204.3 (37.8)	0.18 (0.09)	272.1	1		09-01-2013
JB _{an} -6.5		53	267.2 (2.6)	244.5 (40.4)	0.16 (0.09)	272.6	1		09-01-2013
JB _{an} -6.6		51	267.0 (2.2)	224.4 (38.5)	0.18 (0.09)	272.0	1		09-01-2013
JB _{an} -6.7		47	267.2 (2.0)	220.1 (34.5)	0.16 (0.10)	271.6	2		09-01-2013
JB _{an} -6.8		47	267.5 (2.3)	205.4 (36.5)	0.14 (0.08)	271.8	2		09-01-2013
JB _{an} -6.9		46	267.1 (1.8)	209.4 (32.0)	0.16 (0.10)	271.1	2		09-01-2013
JB _{an} -6.10		45	266.7 (1.5)	202.6 (23.8)	0.14 (0.07)	270.3	1		09-01-2013
JB _{an} -6.11		40	266.8 (1.2)	214.7 (24.2)	0.17 (0.10)	269.6	1		09-01-2013

205

206 Nine snowpits were dug during the February campaign (Table 2), with a mean ρ_{snow} of
 207 225.2 kg m⁻³ and a mean R_{opt} of 0.18 mm. All snowpits were conducted in clearings with
 208 frozen organic soil. On the 15th of February, for a transect of seven snowpits, a complete
 209 set of measurements was taken for each snowpit (SP). An ice lens at a depth of 30 cm
 210 was observed at each SP. In addition to SP measurements, two SEex were conducted in
 211 the transect and two others in JB_{Feb-1} and JB_{Feb-2}.

212

213

Table 2. Same as Table 1, but for James Bay sites in February (JB_{Feb}).

SP	Type	SD (cm)	T_{snow} (K)	ρ_{snow} (kg m ⁻³)	R_{opt} (mm)	T_{soil} (K)	IL	B	Date
JB _{Feb} -1	Forest clearing Organic soil	62	266.9 (2.3)	240.1 (26.2)	0.21 (0.12)	272.8	1		12-02-2013
JB _{Feb} -2		66	265.8 (5.0)	194.7 (37.8)	0.24 (0.10)	273.1	1		13-02-2013
JB _{Feb} -3.1		66	265.3 (3.2)	250.7 (90.7)	0.18 (0.09)	270.8	1	x	15-02-2013
JB _{Feb} -3.2		66	265.6 (3.3)	215.9 (57.8)	0.18 (0.09)	270.5	1		15-02-2013
JB _{Feb} -3.3		65	265.9 (3.0)	228.9 (56.5)	0.11 (0.05)	270.5	1		15-02-2013
JB _{Feb} -3.4		68	266.6 (2.6)	228.1 (54.9)	0.17 (0.09)	271.3	1		15-02-2013
JB _{Feb} -3.5		65	264.0 (4.0)	235.4 (66.0)	0.17 (0.10)	271.0	1	x	15-02-2013
JB _{Feb} -3.6		65	266.5 (4.7)	223.6 (65.8)	0.20 (0.11)	271.3	1		15-02-2013
JB _{Feb} -3.7		64	266.0 (3.2)	209.0 (61.4)	0.18 (0.11)	270.8	1		15-02-2013

214

215 During the March campaign, five snowpits with a mean ρ_{snow} of 278 kg m^{-3} and mean
 216 R_{opt} of 0.26 mm were dug (Table 3). There is a clear increase (70%) of grain size in
 217 March, linked to a strong temperature gradient metamorphism regime typical of such
 218 environments. On March 22nd, a transect of three snowpits was conducted in a clearing
 219 with frozen organic soil.

220

221 **Table 3.** Same as Table 1, but for James Bay sites in March (JB_{Mar}).

SP	Type	SD (cm)	T_{snow} (K)	ρ_{snow} (kg m^{-3})	R_{opt} (mm)	T_{soil} (K)	IL	B	Date
$\text{JB}_{\text{Mar}}-1$	Forest clearing	83	268.2 (3.2)	261.4 (41.0)	0.25 (0.10)	272.0	1		19-03-2013
$\text{JB}_{\text{Mar}}-2$	Organic soil	67	267.5 (2.4)	265.2 (38.2)	0.25 (0.07)	270.9	1		20-03-2013
$\text{JB}_{\text{Mar}}-3.1$	Transect in Forest clearing Organic soil	63	269.3 (0.8)	266.1 (34.9)	0.28 (0.11)	270.5	1		22-03-2013
$\text{JB}_{\text{Mar}}-3.2$		69	271.0 (1.0)	303.1 (28.1)	0.26 (0.09)	272.5	1		22-03-2013
$\text{JB}_{\text{Mar}}-3.3$		67	270.9 (0.8)	294.2 (28.1)	0.25 (0.10)	272.1	1		22-03-2013

222

223 Measurements were also conducted in a forested area (Table 4), where the emission of
 224 the trees that is reflected on the ground contributes to the measured T_{B} (Roy et al., 2012).
 225 For these reasons, these snowpits were treated separately and used to better understand
 226 the influence of tree emission on ground-based radiometric measurements. On January
 227 10th, a transect of eight snowpits was conducted in a forested area as well as transects of
 228 three snowpits on February 14th and March 21st. In addition to the usual snowpit
 229 observations, fisheye pictures (Fig. 2) were taken during the January and February
 230 campaigns to quantify vegetation density. The pictures were binarized to distinguish sky
 231 pixels from tree pixels allowing the estimation of the proportion of pixels (fraction)
 232 occupied by vegetation (χ_{veg}).

233

234 **Table 4.** Same as Table 1, but for James Bay sites, all in forested areas (JB_{veg}).

SP	Type	SD (cm)	T_{snow} (K)	ρ_{snow} (kg m^{-3})	R_{opt} (mm)	T_{soil} (K)	IL	Date
$\text{JB}_{\text{veg}}-1$		62	267.6 (1.8)	222.5 (44.5)	0.14 (0.08)	272.4	1	11-01-2013
$\text{JB}_{\text{veg}}-2.1$	First transect of 30 m	64	267.4 (2.7)	202.6 (43.3)	0.18 (0.09)	273.3	1	10-01-2013
$\text{JB}_{\text{veg}}-2.2$		67	269.0 (2.3)	211.6 (49.9)	0.15 (0.09)	273.3	1	10-01-2013
$\text{JB}_{\text{veg}}-2.3$		60	268.3 (3.1)	201.4 (58.5)	0.16 (0.09)	273.4	1	10-01-2013
$\text{JB}_{\text{veg}}-2.4$		60	267.6 (2.1)	197.2 (40.0)	0.19 (0.10)	272.4	1	10-01-2013
$\text{JB}_{\text{veg}}-2.5$		65	267.1 (2.5)	200.7 (48.9)	0.15 (0.08)	272.8	1	10-01-2013
$\text{JB}_{\text{veg}}-2.6$		60	266.3 (2.0)	195.5 (59.8)	0.15 (0.08)	271.9	1	10-01-2013
$\text{JB}_{\text{veg}}-2.7$		56	268.4 (2.5)	199.4 (36.5)	0.15 (0.09)	272.9	1	10-01-2013
$\text{JB}_{\text{veg}}-2.8$		68	268.1 (2.9)	205.4 (45.2)	0.14 (0.08)	273.1	1	10-01-2013
$\text{JB}_{\text{veg}}-3.1$	Second transect of 6 m	78	267.0 (2.8)	231.6 (44.1)	0.19 (0.10)	272.4	2	14-02-2013
$\text{JB}_{\text{veg}}-3.2$		78	267.4 (2.4)	217.0 (55.8)	0.19 (0.10)	272.6	2	14-02-2013
$\text{JB}_{\text{veg}}-3.3$		75	267.5 (2.2)	222.0 (62.1)	0.19 (0.12)	272.4	1	14-02-2013
$\text{JB}_{\text{veg}}-4.1$	Third	88	268.1 (1.5)	281.4 (55.3)	0.20 (0.11)	271.9	3	21-03-2013

JB _{veg} -4.2	transect of 6 m	88	269.9 (1.5)	283.2 (42.8)	0.22 (0.12)	272.9	3	21-03-2013
JB _{veg} -4.3		87	271.5 (1.0)	288.8 (43.7)	0.28 (0.12)	272.9	3	21-03-2013

235

236



237

238

239

240

241

242

243

244

245

246

247

248

249

250

251

Fig. 2. Fisheye pictures for JBveg-3.3 (left) and JBveg-2.2 (right) sites, showing the sky view proportion around the SBR site measurements.

2.1.2 Umiujaq

An intensive measurement campaign was conducted in January 2014 (21st to 28th) in the region of Umiujaq. All the measurements were conducted in a tundra environment except for the Umi-3 site, which was located in a clearing (Table 5). The tundra sites were characterized by typical dense snow drift layers near the surface that fall into the bridging limits of 0.4 and 0.6 for the ice fraction as defined by Dierking et al. (2012) (see Sect. 2.2.2). Furthermore, one to two ice lenses were observed at the UMI-1, UMI-2 and UMI-4 sites.

Table 5. Same as Table 1, but for Umiujaq sites (UMI).

SP	Type	SD (cm)	T _{snow} (K)	ρ_{snow} (kg m ⁻³)	R _{opt} (mm)	T _{soil} (K)	IC	B	Date
UMI-1	Tundra	35	253.9 (2.6)	361.8 (54.4)	0.15 (0.12)	258.4	2	x	22-01-2014
UMI-2		70	256.2 (4.6)	379.0 (40.5)	0.18 (0.09)	265.2	2	x	23-01-2014
UMI-3	Forest clearing	132	263.5 (5.8)	319.0 (51.2)	0.18 (0.08)	271.8	0	x	24-01-2014
UMI-4	Tundra	57	256.9 (4.2)	280.7 (46.5)	0.23 (0.11)	264.4	1		25-01-2014
UMI-5		93	254.0 (3.9)	350.6 (42.3)	0.19 (0.09)	261.6	0	x	26-01-2014

252

253

254

255

256

2.2 Models

The study uses the DMRT-ML model to simulate the microwave emission of snow-covered surfaces (Brucker et al. 2011; Picard et al., 2013). It is a multilayer

257 electromagnetic model based on the DMRT theory (Tsang and Kong, 2001). The theory
258 assumes that a snow layer is composed of ice spheres where the effective permittivity is
259 calculated using the first-order quasi-crystalline approximation and the Percus-Yevick
260 approximation. The propagation of energy between the different layers is calculated with
261 the Discrete Ordinate Radiative transfer (DISORT) method as described in Jin et al.
262 (1994). In this paper, the propagation of electromagnetic radiation was calculated for 64
263 streams.

264

265 The snowpit measurements (ρ_{snow} , T_{snow} , T_{soil} and R_{opt}) were integrated as input to the
266 model to simulate snow microwave emission. However it was shown in previous studies
267 (Brucker et al. 2011; Roy et al., 2013; Picard et al. 2014) that using R_{opt} was inadequate
268 as input to DMRT-ML. As such, a scaling factor of $\phi = 3.3$ assuming non-sticky snow
269 grains from Roy et al. (2013) for the seasonal snowpack is thus applied to get an effective
270 radius in the microwave range (R_{eff}):

271

$$272 \quad R_{\text{eff}} = R_{\text{opt}} \cdot \phi \quad (2)$$

273

274 Roy et al. (2013) shows that the need for a scaling factor in DMRT-ML could be related
275 to the grain size distribution of snow and the stickiness between grains, which leads to an
276 increase of the R_{eff} .

277

278 The atmospheric downwelling T_{B} that is reflected by the snow surface to the radiometer
279 was modeled using the millimeter-wave propagation model (Liebe et al., 1989)
280 implemented in the Helsinki University of Technology (HUT) snow emission model
281 (Pulliainen et al., 1999). The atmospheric model was driven with the air temperature and
282 air moisture of the atmospheric layer above the surface from the 29 North American
283 Regional Reanalysis (Mesinger et al., 2006) atmospheric layers.

284

285 **2.2.1 Ice lenses**

286

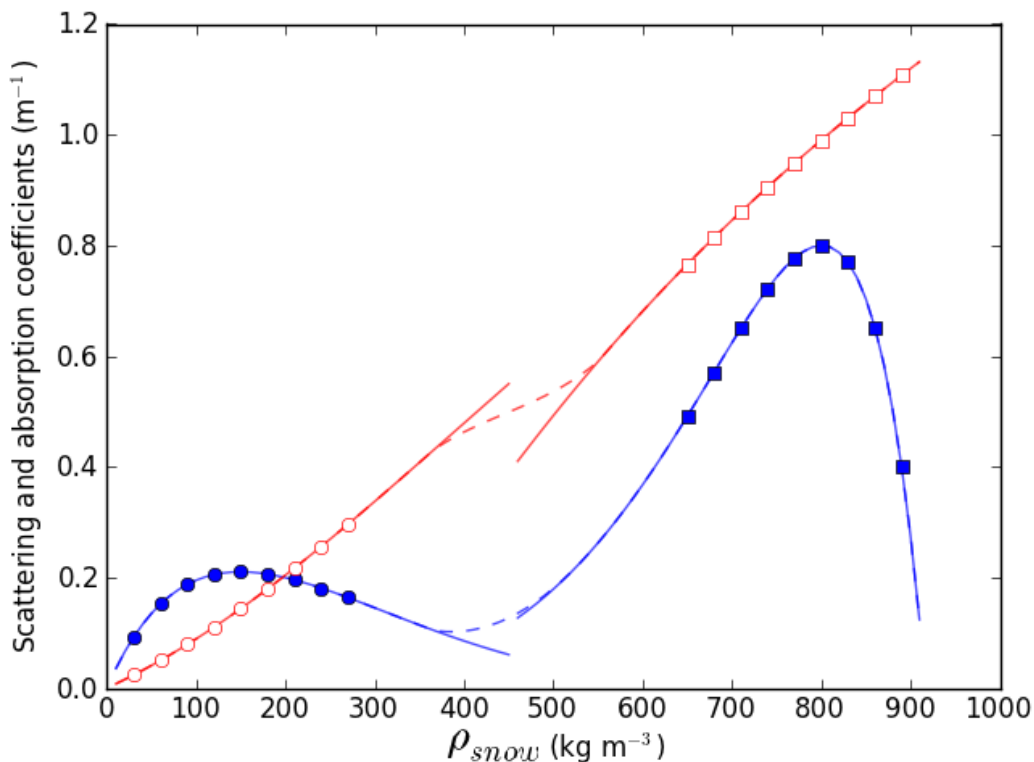
287 The microwave signal is very sensitive to ice lens formation within a snowpack at H-pol
288 (Montpetit et al., 2013; Rees et al., 2010; Lemmetyinen et al., 2010). To simulate the ice
289 lenses present in this study's database (see Tables 1 to 5) using DMRT-ML, snow layers
290 with a high density of 900 kg m^{-3} close to the density of pure ice (917 kg m^{-3}) and a null
291 snow grain size were integrated into the snowpack input file where ice lenses were
292 observed. The value of 900 kg m^{-3} was chosen because only pure ice lenses were
293 observed. To keep the same total snow depth, the adjoining layers were adjusted by
294 removing 0.5 cm of the layer above and below the ice layer. However, an analysis of the
295 effect of ice lens density on T_{B} simulations will be conducted in Sect. 3.2.4. Because
296 coherence is neglected in DMRT-ML (Matzler, 1987), the ice lens thickness has a
297 negligible effect on simulated T_{B} . Hence, because no precise measurements of ice lens
298 thickness were performed in the field, ice lens thickness was set to 1 cm in DMRT-ML.

299

300
301
302
303
304
305
306
307
308
309
310
311
312
313
314
315
316
317
318
319
320

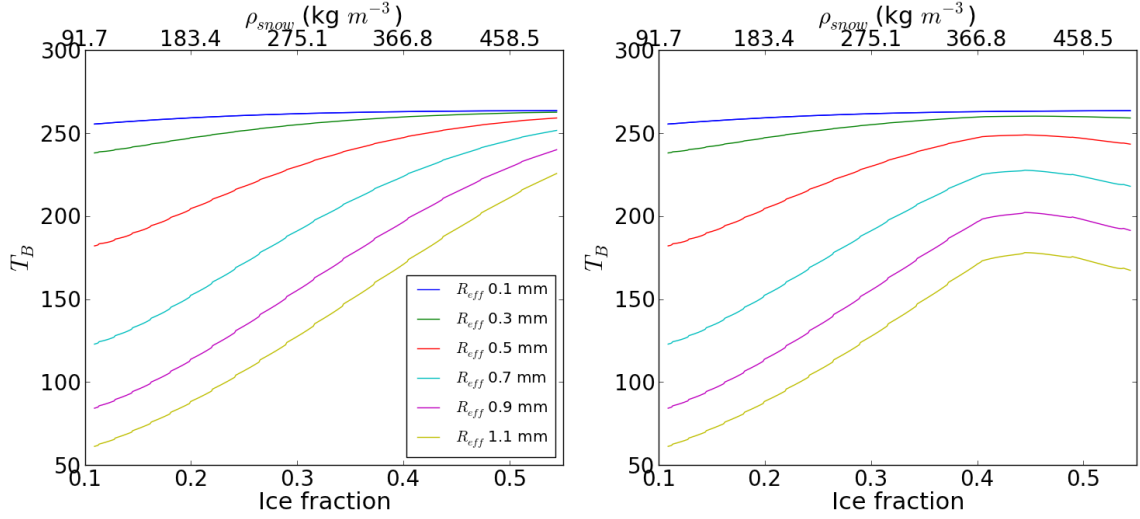
2.2.2 Bridging

It has been shown that DMRT theory is in agreement with numerical solutions of the 3-D Maxwell equations up to a density of 275 kg m^{-3} (ice fraction of 0 - 0.3) (Tsang et al., 2008), which is a relatively low density for snow. Although most of the applications of DMRT theory concern snow, DMRT can be applied to other dense media such as bubbly ice (Dupont et al., 2014). In this case, the background is pure ice, and the scatterers are air spheres to represent bubbles. To the best of our knowledge, no validity tests have been done in this configuration; but if we assume a similar range of validity in terms of volume fraction of scatterers, the DMRT theory would be valid in the range 0.7 – 1 for the ice fraction, that is $642 - 917 \text{ kg m}^{-3}$. Even in this case, a large range of intermediate densities remains for which the absorption and scattering coefficients might not be accurate. Following Dierking et al. (2012), an empirical extrapolation of these coefficients from a spline fitted in both validity ranges was implemented to calculate coefficients for a layer with an ice fraction between 0.4 ($\rho_{\text{snow}} = 367 \text{ kg m}^{-3}$) and 0.6 ($\rho_{\text{snow}} = 550 \text{ kg m}^{-3}$) (Fig. 3). As an example, the bridging leads to a decrease of T_B at 37 GHz for high snow density ($> 350 \text{ kg m}^{-3}$) related to the increase of scattering (Fig. 4). In the following, this approach is denoted as ‘bridging’ and the limits will be set at 0.4 and 0.6 for the ice fraction following the study of Dierking et al. (2012).



321
322
323
324

Fig. 3. Absorption (red) and scattering (blue) coefficients as a function of ρ_{snow} at 37 GHz ($T_{\text{snow}} = 260 \text{ K}$, $T_{\text{soil}} = 270 \text{ K}$, $SD = 1.0 \text{ m}$ and $R_{\text{eff}} = 0.3 \text{ mm}$). The dotted lines show the bridging implementation for an ice fraction between 0.4 and 0.6.



326

327

Fig. 4. T_B without (left) and with the bridging implementation (right) at 37 GHz (V-pol) for different R_{eff} ($T_{\text{snow}} = 260$ K, $T_{\text{soil}} = 270$ K and $SD = 1.0$ m).

328

329

330

331

332

333

334

335

336

337

338

339

2.2.3 Soil model

340

341

342

343

344

Soil reflectivity models are included in DMRT-ML to account for the soil contribution to the measured T_B . In this paper, the Wegmüller and Mätzler (1999) soil reflectivity model improved for frozen soil by Montpetit et al. (2015) is used. The Wegmüller and Mätzler (1999) model for incidence angles lower than 60° is described by:

345

$$\Gamma_{f,H-pol} = \Gamma_{f,H}^{Fresnel} \exp(-(k\sigma)^{\sqrt{-0.1\cos\theta}}) \quad (3)$$

346

347

$$\Gamma_{f,V-pol} = \Gamma_{f,H} \cos \theta^\beta \quad (4)$$

348

349

350

351

352

353

354

where $\Gamma_{f,p}$ is the rough soil reflectivity at a frequency f and polarization p (H-pol or V-pol) by its smooth Fresnel reflectivity in H-Pol ($\Gamma_{f,H}$), which depends on the incidence angle (θ) and the real part of the soil permittivity (ϵ'), weighted by an attenuation factor that depends on the standard deviation in height of the surface (soil roughness, σ), the measured wavenumber (k) and a polarization ratio dependency factor (β). The values of ϵ' , σ and β at 11, 19 and 37 GHz inverted by Montpetit et al. (2015) for frozen soil (Table

355 6) were used in this study. Montpetit et al. (2013) used independent snow free ground-
 356 based radiometer angular measurements taken at James Bay site in 2013 (same
 357 campaign). The parameters were also validated over Umiujaq (same campaign) from
 358 snow removal experiment.

359
 360

Table 6. Main parameters used in DMRT-ML

Frequency (GHz)	ϵ	β	ϕ	fluxes	σ (cm)	θ (°)
11	3.197	1.077	3.3	64	0.193	55
19	3.452	0.721				
37	4.531	0.452				

361

362 **3. Results**

363

364 In this section, the impact of model improvements (ice lenses and bridging) is first
 365 presented. Afterward, the evaluation of the effect of the different sources (soil, snow
 366 grain size, snow density, ice lenses and vegetation) on T_B is shown.

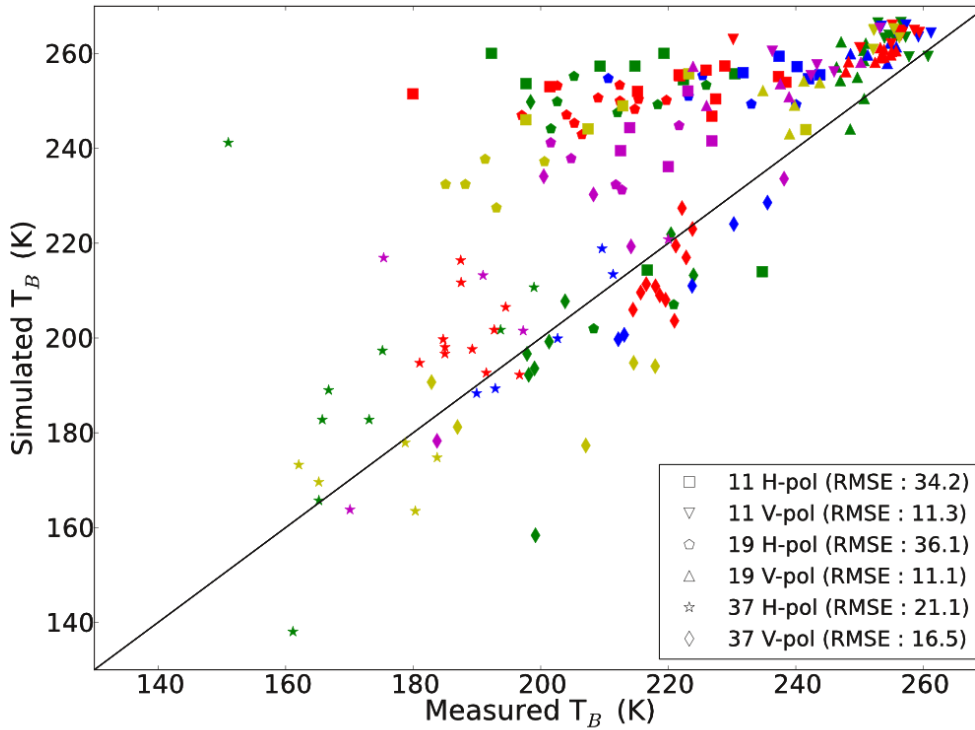
367

368 **3.1 Model validation and improvement**

369

370 Initial simulations ignoring the presence of ice lenses and bridging show a clear
 371 overestimation of T_B mostly at H-pol. The observed root mean square error (RMSE) is
 372 greater than 35 K at 11 and 19 GHz and greater than 20 K at 37 GHz (Fig. 5). There is
 373 also a positive bias for T_B at 11 and 19 GHz at V-pol. In this section, the effect of ice
 374 lenses on T_B is evaluated, while the bridging implementation was tested on snowpits data.

375



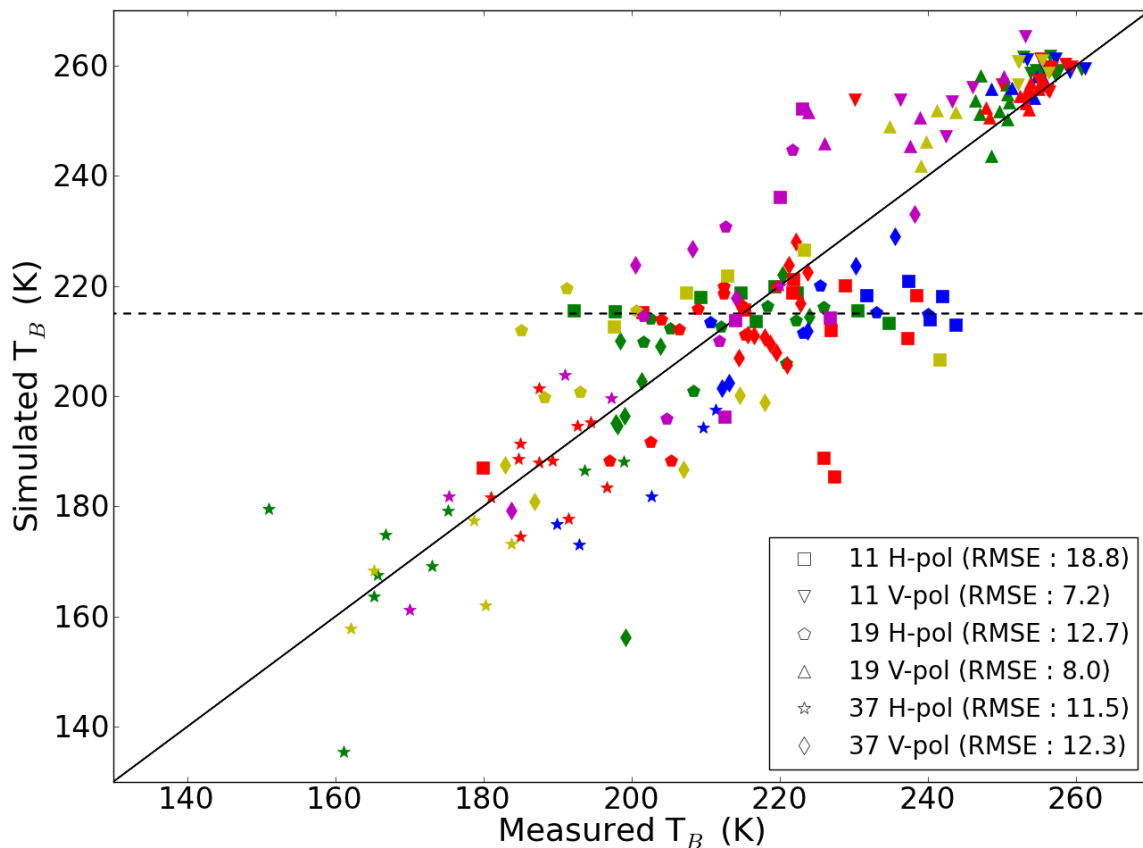
376
 377 **Fig. 5.** T_B simulated without ice lenses in DMRT-ML and bridging. RMSE (K) between
 378 measured and simulated T_B are given in parentheses. The symbol types correspond to the
 379 frequency and colors to the sites: Red = $JB_{Jan-transsect}$; Green = $JB_{Jan-others}$; Blue = JB_{Feb} ;
 380 Yellow = JB_{Mar} ; Magenta = UMI.

381 382 3.1.1 Ice lenses

383
 384 Simulations including observed ice lenses were conducted on all snowpits (Fig. 6)
 385 leading to a strong decrease in simulated T_B H-pol (up to 40 K). At H-pol, the RMSE are
 386 thus improved by 15.4, 23.4 and 9.3 K at 11, 19 (initially > 35 K) and 37 GHz (initially >
 387 20 K) respectively. The ice lenses also slightly decrease the bias measured at V-pol for all
 388 frequencies leading to a RMSE improvement of 3 to 4 K. These results show that a
 389 simple ice lens implementation in DMRT-ML helps to simulate the strong reflection
 390 component of ice lenses (decrease of snowpack emissivity), leading to improved
 391 simulations of T_B .

392
 393 However, a large variability (190 to 245 K) in T_B observations at H-pol at 11 and 19 GHz
 394 is not reproduced by the simulations (dotted black line in Fig. 6). This feature suggests
 395 some limitations of ice lens and/or snow layering modeling in DMRT-ML that can be
 396 related to the fact that coherence effect is not taken into account. Note that this
 397 underestimation of T_B spatial variability is not related to the soil as it is demonstrated in
 398 Sect. 3.2.1. The modeling uncertainties related to ice lenses will be discussed more
 399 specifically in Sect. 3.2.4.

400



402

403

404

405

406

407

408

409

410

Fig. 6. T_B simulated with ice lenses included in DMRT-ML, but without bridging. The symbol types correspond to the frequency and colors to the sites: Red = $JB_{Jan-transect}$; Green = $JB_{Jan-others}$; Blue = JB_{Feb} ; Yellow = JB_{Mar} ; Magenta = UMI. The dotted black line represents the T_B where the simulations underestimated the spatial variability at 11 and 19 GHz H-pol.

408

409

3.1.2 Bridging

410

411

412

413

414

415

416

417

418

419

420

421

422

423

To test the bridging parameterization (see Sect 2.2.2), we used 13 tundra sites from the Churchill tundra database (Roy et al., 2013), 4 from Umiujaq and 2 from the James Bay snowpits. In each case, at least one snow layer with a snow density higher than 367 kg m^{-3} (ice fraction of 0.4: Dierking et al., 2012) is used. For each of the 19 sites studied, simulations at 37 GHz (the most sensitive frequency to snow) with and without the bridging implementation were conducted (all input parameters kept the same). The bridging has a relatively modest impact on simulations with an improvement in the RMSE of between 2 and 4 K at tundra sites (Umiujaq and James Bay). The greatest improvements are found for deep drifted tundra snowpits where there is a very thick wind slab with high ρ_{snow} and small rounded grains are present at the top of the snowpack.

421

422

3.2 Signal contributions and modeling uncertainties

423

424 In the following, all DMRT-ML simulations consider the bridging implementation and
 425 include the observed ice lenses. Table 7 shows the overall RMSE for all campaigns that
 426 are described in Sect. 3.3.1 to 3.3.4. The RMSE values oscillate between 7.8 and 21.5 K
 427 at H-pol (Table 7). Since V-pol is less affected by layering in the snowpack at 11 GHz
 428 and 19 GHz, the RMSE are generally lower (between 3.5 and 14.4 K), while the RMSE
 429 at 37 GHz are similar at V-pol and H-pol. This is due to the higher sensitivity of higher
 430 frequencies to snow grain scattering when compared to the lower frequencies that are less
 431 affected by stratigraphy. Table 7 also suggests that the inclusion of bridging only
 432 decreases the RMSE by 0.5 K and 0.3 K at 37 GHz at H-pol and V-pol respectively (see
 433 Fig. 5). These RMSE will thus be used as a reference to quantify the effect of spatial
 434 variability and uncertainty in measurements on the T_B simulations.

435

436 **Table 7:** Overall RMSE (K) between measured and simulated T_B for all sites considering
 437 ice lenses and bridging in DMRT-ML.

	JB _{Jan}	JB _{Feb}	JB _{Mar}	UMI	All
11H	21.5	13.6	18.2	14.3	18.8
11V	6.4	5.5	6.3	9.8	7.2
19H	11.7	8.7	19.8	11.2	12.7
19V	3.5	5.7	9.2	13.4	8.0
37H	12.1	15.1	9.7	9.7	11.5
37V	7.8	15.3	14.4	16.8	12.3

438

439

440 3.2.1 Soil roughness

441

442 The analysis of small-scale soil variability in modeling the T_B of snow-covered surfaces
 443 is conducted using the SEex from the transect during the JB_{Jan} (mineral soil) and JB_{Feb}
 444 campaigns (organic soil). The JB_{Jan} SEex data represent the variability within a 30 m
 445 transect in a relatively homogeneous mineral soil area (quarry). The JB_{Feb} SEex were
 446 conducted at four different locations in clearings with organic soil and within about 1 km
 447 from each other. The strategy behind the evaluation of the small-scale spatial variability
 448 on snow-covered T_B is to first calculate the soil emission variability (optimization of σ)
 449 from SEex measurements. This variability is then introduced in the simulations with
 450 snow-covered surfaces to evaluate the sensitivity of T_B to variability in the emission of
 451 frozen soil.

452

453 For each SEex measurement, the surface roughness parameter σ was optimized using the
 454 three frequencies and both polarizations for bare soil measurements. The σ value was
 455 changed by increments of 0.01 cm, up to 1 cm (Eq. 3 and 4) and the associated $RMSE_\sigma$
 456 was calculated as a function of the measured T_B (T_{Bmes}) and simulated T_B (T_{Bsim}) in V-pol
 457 and H-pol as follows:

458

$$459 \quad RMSE_\sigma = \sqrt{\frac{\sum_{j=1}^3 \sum_{i=1}^N (T_{Bsim;i}^{jV} - T_{Bmes;i}^{jV})^2 + (T_{Bsim;i}^{jH} - T_{Bmes;i}^{jH})^2}{6N}} \quad (5)$$

460

461 where j corresponds to the frequencies ($j=1,2,3$ respectively for 11, 19 and 37 GHz) and i
462 corresponds to the sites. The optimal σ was determined by the lowest $RMSE_\sigma$ (Eq. 5)

463 value for all sites at JB_{Jan} and JB_{Feb} .

464

465 The optimization was also done for each site individually to estimate the spatial
466 variability in σ . The results presented in Fig. 7 show that a clear minimum in the $RMSE_\sigma$

467 can be found at every site. Fig 7 (right) shows that the optimal σ at $JB_{Jan-transsect}$ values are

468 located between 0.22 and 0.54 cm, while 0.31 is found for all 5 sites. The variability can
469 be explained by the variation of the gravel size that affects the surface roughness. For

470 JB_{Feb} , the observed spatial variability is more significant with variations ranging between

471 0.195 cm and 1.987 cm with an optimized $\sigma = 0.411$ cm for all 4 sites (Fig. 7 left).

472 However, one should be careful in interpreting these results as the optimization could

473 also compensate for uncertainties in the permittivity of frozen ground. Nevertheless,

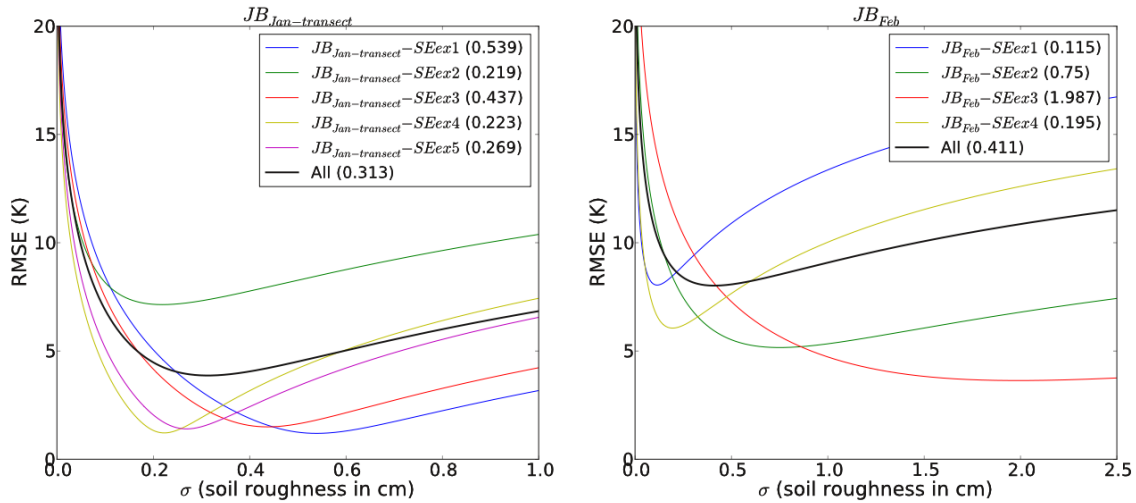
474 because the minimal and maximal values of optimized σ are taken, this does not affect

475 our main goal, which is to estimate the variability in snow-covered T_B introduced by the

476 soil in the model. Furthermore, as mentioned in Sect. 2.2.3, the permittivity used in this

477 study were retrieved at the same site as this study.

478



479

480 **Fig. 7.** $RMSE_\sigma$ for bare frozen soil sites (snow excavation experiment, SEex) as a

481 function of soil roughness (σ) for (left) $JB_{Jan-transsect}$ and (right) JB_{Feb} . The optimized σ for
482 each site is given in parentheses.

483

484 We evaluated the small-scale spatial variability of soil emissivity resulting from the

485 observed roughness variability. For the sites with observations taken with snow on the

486 ground (Tables 1, 2, 3 and 5, for both campaigns), we simulated the T_B with DMRT-ML

487 considering the lowest and highest optimized σ (see Fig. 7). Note that we have not used

488 the standard deviation of σ that would have led to negative values. Fig. 8 (left) shows that

489 the T_B sensitivity to the variation of soil roughness is very weak. T_B variations of 0.5 K

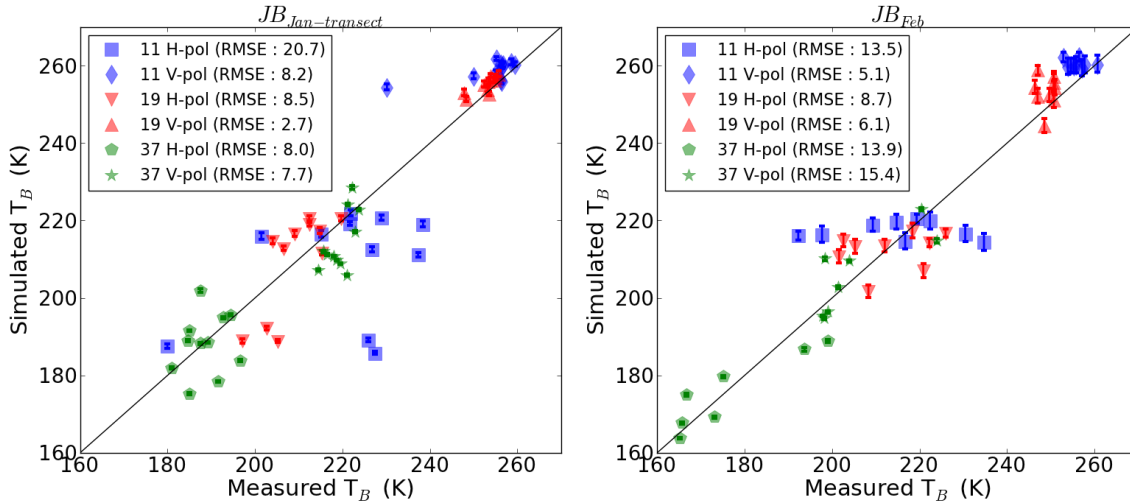
490 and 1.3 K were observed at the $JB_{Jan-transsect}$ site where the soil properties were more

491 homogeneous (mineral soil), while a variation of 0.7 K to 3.8 K was measured at the

492 JB_{Feb} site with organic soil (Table 8). The sensitivity is higher at 11 and 19 GHz because

493 the soil emission is less attenuated by snow grain scattering. We also performed the same

494 calculation without the ice lens implementation where results are similar (less than 1 K
 495 change) suggesting that despite a potential low transmissivity, ice lenses are not
 496 responsible for the attenuation of the soil upwelling emission.
 497



498 **Fig. 8.** Sensitivity of snow-covered surface T_B to the variation of soil roughness (σ) for
 499 (left) $JB_{Jan-transect}$ and (right) JB_{Feb} . The error bars show the variation of T_B for maximum
 500 and minimum optimized σ derived from SEx during both campaign (Fig. 7). The RMSE
 501 (K) values correspond to the retrievals using the initial (Table 6) σ value.
 502

503 **Table 8:** T_B sensitivity (ΔT_B) (K) associated with the small-scale variability of soil
 504 roughness (σ).
 505

	$JB_{Jan-transect}$	JB_{Feb}
11H	1.3	3.8
11V	1.3	3.8
19H	1.2	3.2
19V	1.4	3.5
37H	0.5	0.7
37V	0.6	0.7

506 The results show that the soil small-scale spatial variability is much lower than the RMSE
 507 for most of the frequencies and polarizations (Tables 7 and 8). However, for 11 and 19
 508 GHz at V-pol, the soil-induced variability calculated during JB_{Feb} campaign leads to ΔT_B
 509 values (Table 8) similar to the measured RMSE (Table 7). Hence, the modeling error
 510 cannot be solely explained by small-scale variability in the emissivity of frozen soil,
 511 except possibly for 11 and 19 GHz at V-pol. However, these conclusions are only valid
 512 for frozen soils, but the higher dielectric contrast of thawed soil would have a greater
 513 impact on the emissivity of snow-covered surfaces.
 514

515 3.2.2 Snow grain size

516 To test the sensitivity of the simulations to the grain size (SSA) measurement errors, the
 517 simulations considered an error of 12% in SSA when using the shortwave infrared
 518 reflection measurement approach as reported in Gallet et al. (2009). Hence two
 519 simulations were conducted: one with all SSA data along the profile increased by 12%
 520
 521

522 ($T_{BSSA+12\%}$), and one with all SSA data decreased by 12% ($T_{BSSA-12\%}$). From these two
523 simulations, the variation of T_B related to SSA errors (ΔT_{BSSA} : $T_{BSSA+12\%} - T_{BSSA-12\%}$) was
524 calculated, keeping in mind that this should be the maximum ΔT_B error, since the
525 variations in SSA are all in the same direction for the whole profile. The soil
526 parameterization is kept the same for all sites (see Table 6).

527

528 Figure 9 shows the error bars related to a variation of + 12% in SSA (upper bars: higher
529 SSA leads to smaller grains and less scattering) and - 12 % (lower bars: lower SSA leads
530 to larger grains and more scattering). The results show that 37 GHz is the most sensitive
531 to the grain size with variations between 16.2 K and 27.4 K (Table 9). The variations are
532 generally higher at V-pol, which has a higher penetration depth with less sensitivity to
533 stratification and ice lenses. As such, 37 GHz is more influenced by large depth hoar
534 grains at the bottom of the snowpack. Hence, because the relationship between the
535 scattering and the particle size reaches a maximum sensitivity within the particle range
536 (Picard et al. 2013), the variation of 12% for depth hoar SSA will cause a higher increase
537 of ΔT_{BSSA} . In all cases, ΔT_{BSSA} are higher than the RMSE (Table 7) suggesting that grain
538 size can explain the uncertainty in the T_B simulations.

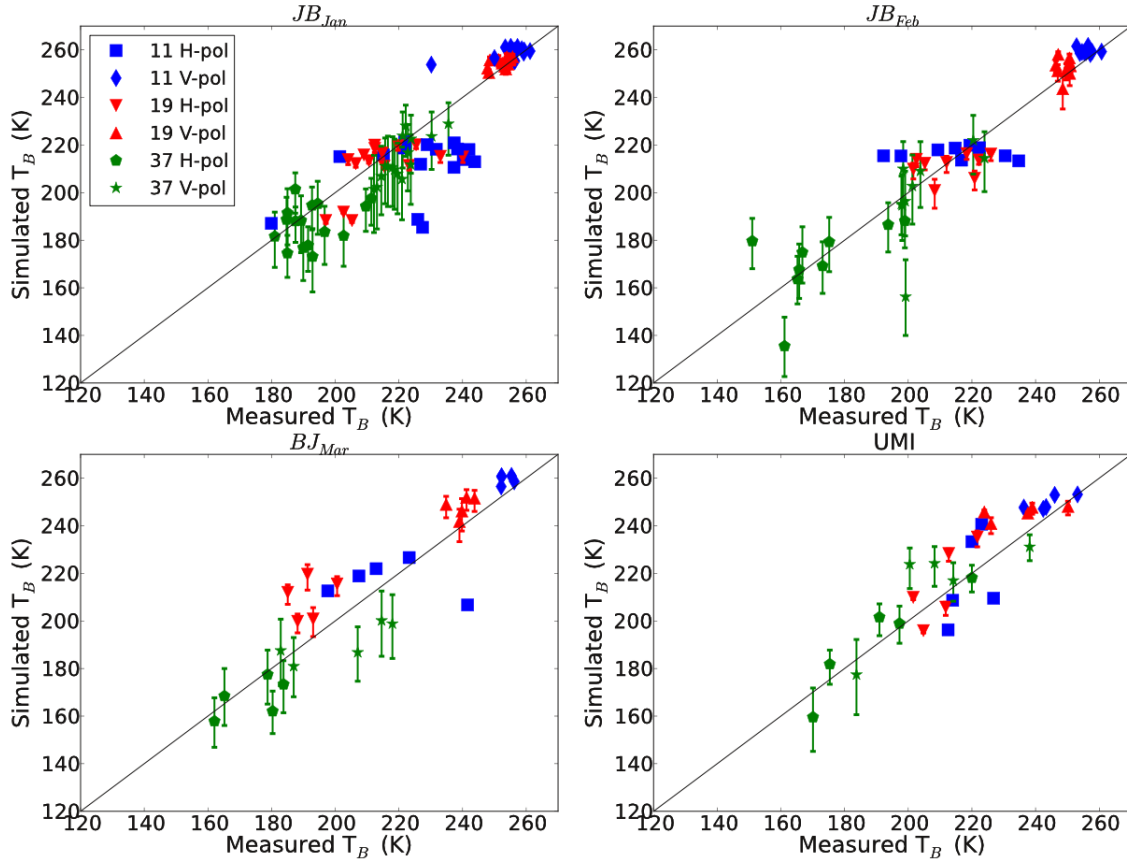
539

540 At 19 GHz, there is an increase in ΔT_{BSSA} of about 7 K at V-pol and H-pol during the
541 three James Bay campaigns. This increase of ΔT_{BSSA} is linked to snow grain
542 metamorphism (Colbeck, 1983) that tends to increase the particle size through the winter
543 (see Table 1, 2 and 3). With a higher sensitivity on the particle range and the dependence
544 of scattering to the particle size, the variation of large grains will increase ΔT_{BSSA} . This
545 phenomenon shows that at 19 GHz, the effect of SSA measurement uncertainty on T_B
546 depends on the type of grains. For small snow grains in January, the error in SSA is small
547 compared to the RMSE, which is not the case in March where the error is closest to the
548 RMSE in the presence of larger grains. A very small increase of ΔT_{BSSA} is also seen at 11
549 GHz, but with much lower ΔT_{BSSA} (less than 1 K). These results show that scattering is
550 negligible at 11 GHz for seasonal snow, even with large grains such as depth hoar.

551

552 We assessed average variation in T_B resulting from 100 runs with random error between
553 $\pm 12\%$ applied to SSA for each layer and snowpit. As expected, the results show that the
554 variations between initial simulation and simulation with random error on SSA are
555 significantly lower than those shown in Table 9. With random error applied on SSA
556 measurements, the variations are lower than 1 K at 11 and 19 GHz, and between 2 and 3
557 K at 37 GHz. These values give the lower limits of T_B error related to SSA uncertainties,
558 while values in Table 9 give the highest limit of the variation in T_B .

559



560
 561 **Fig. 9.** T_B sensitivity associated to the error of SSA measurements (12%) for the James
 562 Bay (three dates) and Umiujaq sites.

563
 564 **Table 9:** T_B sensitivity (ΔT_{BSSA} : $T_{BSSA+12\%} - T_{BSSA-12\%}$) (K) associated with the error of
 565 SSA measurements

	JB _{Jan}	JB _{Feb}	JB _{Mar}	UMI
11H	0.3	0.7	1	0.5
11V	0.3	0.7	1.1	0.5
19H	2.8	6.5	10	4.5
19V	3.3	6.9	11.1	4.5
37H	21.2	21.6	22.5	16.2
37V	27.4	26.7	25.9	18.6

566
 567 **3.2.3 Snow density**

568
 569 A similar analysis was conducted to evaluate the T_B sensitivity to an error in ρ_{snow} of +/-
 570 10% ($T_{B\rho_{\text{snow}+10\%}}$ and $T_{B\rho_{\text{snow}-10\%}}$). The ice lens density was left at 900 kg m^{-3} and the
 571 variations in T_B related to the ρ_{snow} error ($\Delta T_{B\rho_{\text{snow}}}$: $T_{B\rho_{\text{snow}+10\%}} - T_{B\rho_{\text{snow}-10\%}}$) were
 572 calculated.

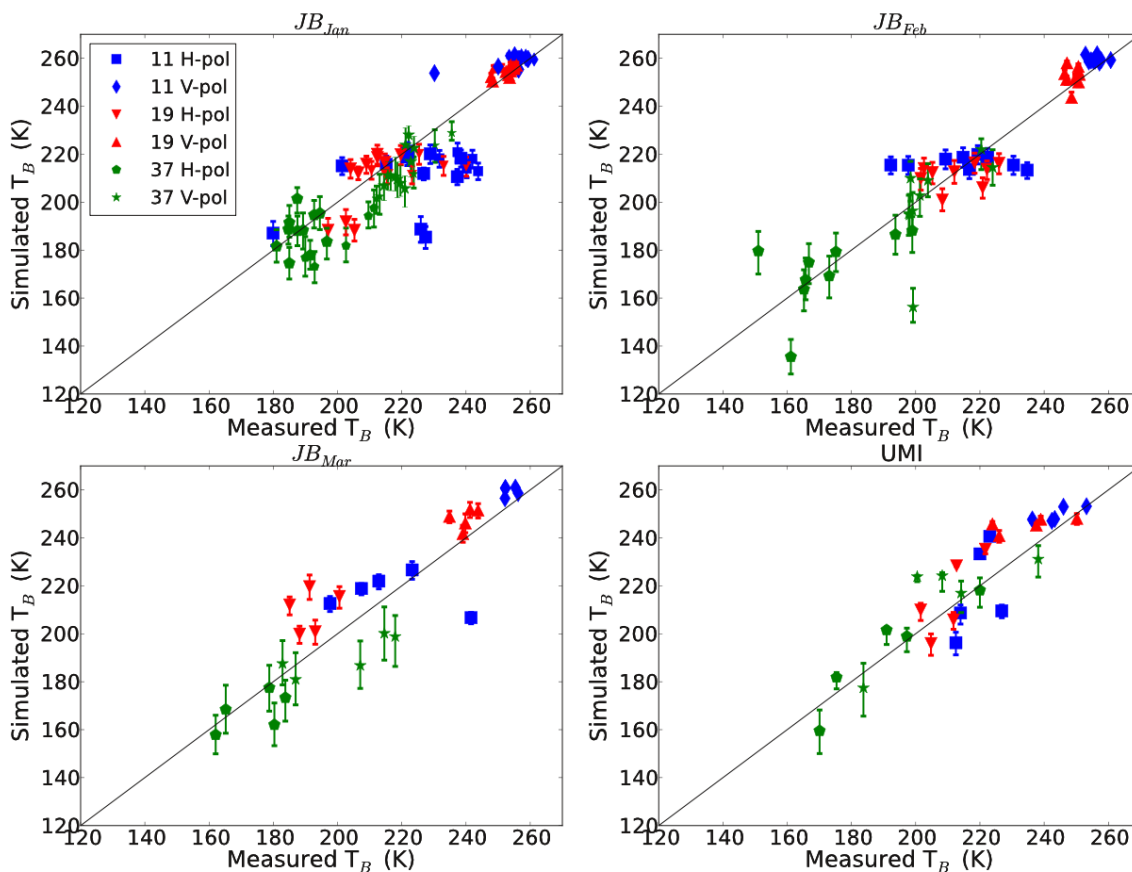
573
 574 The highest sensitivity to ρ_{snow} is seen at 37 GHz (Fig. 10). The $\Delta T_{B\rho_{\text{snow}}}$ are about 13 K
 575 during the JB_{Jan} campaign and increase to 20 K for JB_{Mar} (Table 10). Again, this increase
 576 is explained by the growth in snow grain size due to snow metamorphism that leads to
 577 lower density values. In the given range of sphere sizes and ρ_{snow} at 37 GHz, the impact

578 of ρ_{snow} on T_B increases with a larger grain size (Fig. 3). These results show that the effect
 579 of ρ_{snow} at 37 GHz on DMRT-ML simulations depends on grain size and evolves
 580 throughout the winter due to snow metamorphism. It should, however, be noted that if the
 581 ice fraction limits of the bridging (Sect. 3.1.2) were extended to a lower ice fraction
 582 density, the impact for high ρ_{snow} would be lower or even the opposite, because of the
 583 increase in scattering due to bridging. Table 10 shows that $\Delta T_{B\rho_{\text{snow}}}$ are of the same
 584 magnitude as RMSE. Hence, depending on the grain size, ρ_{snow} can explain part of the
 585 error in the simulations.

586

587 At 11 and 19 GHz, the highest $\Delta T_{B\rho_{\text{snow}}}$ are found at H-pol with values around 7 K
 588 (Table 10). These highest values are related to the change in the permittivity discontinuity
 589 between layers, mostly at interfaces around the ice lenses leading to a change in the
 590 reflectivity at the different interfaces (Montpetit et al., 2013). Because V-pol is less
 591 affected by horizontal layering, the effect is smaller. Hence, the effect of ρ_{snow} uncertainty
 592 on T_B is lower than the measured RMSE at 11 and 19 GHz, but has a significant impact
 593 on T_B at H-pol. These results are in agreement with studies that show that the microwave
 594 polarization ratio (H-pol/V-pol) can potentially be used for snow density retrievals
 595 (Champollion et al., 2013; Lemmetyinen et al., submitted).

596



597

598 **Fig. 10.** T_B sensitivity associated with the error in snow density measurements ($\pm 10\%$).

599 The ice lens density remains at 900 kg m^{-3} .

600

601 **Table 10.** T_B sensitivity ($\Delta T_{B\rho_{\text{snow}}} : T_{B\rho_{\text{snow}+10\%}} - T_{B\rho_{\text{snow}-10\%}}$) (K) associated with the error
 602 in snow density measurements

	JB _{Jan}	JB _{Feb}	JB _{Mar}	UMI
11H	7.6	7.5	5.6	6.1
11V	1.4	1.4	2.1	1.9
19H	8	8.8	8.3	6.2
19V	2.4	3.2	6.7	3.6
37H	13.5	16.5	18.4	11.6
37V	12.6	15.3	21.4	13.4

603

604

605 3.2.4 Ice lenses

606

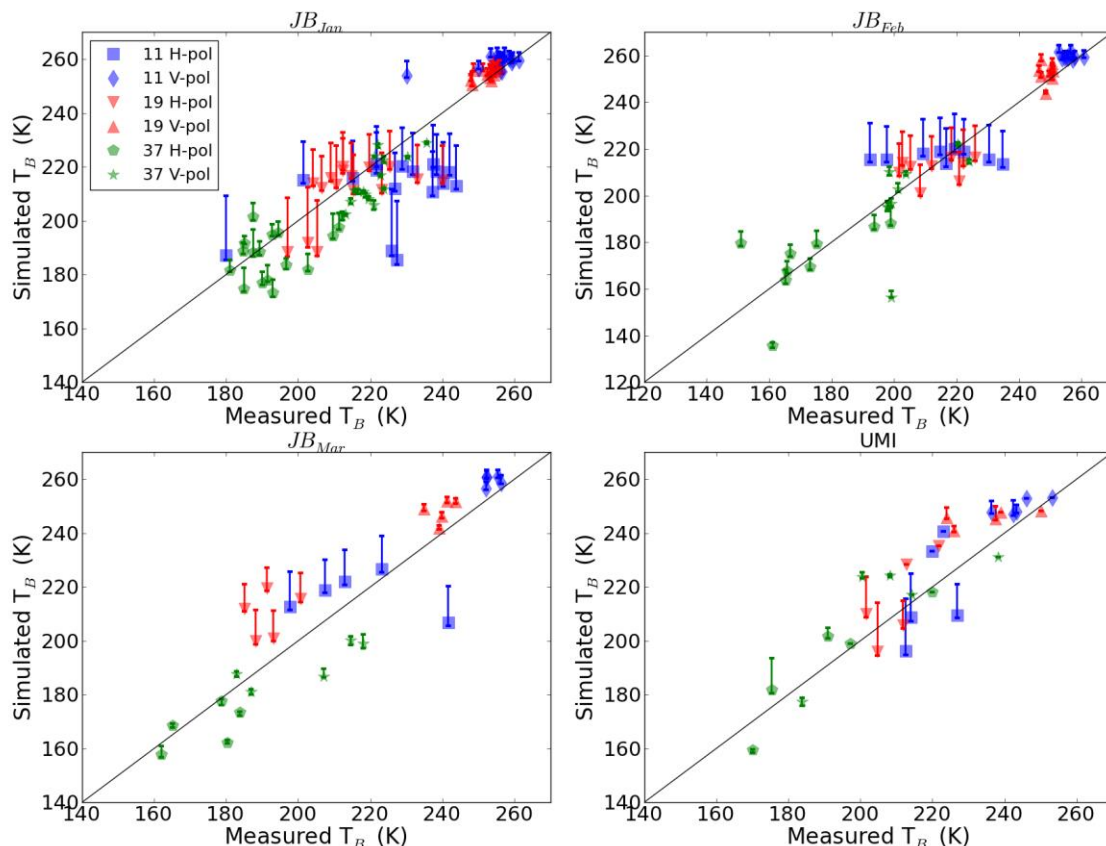
607 While including ice lenses in DMRT-ML significantly reduces the RMSE (section 3.1.1),
 608 the underestimation of T_B variability remains strong at 11 and 19 GHz. Given that the
 609 remaining bias cannot be explained by the soil, grain size or ρ_{snow} (Sect. 3.3.1, 3.3.2 and
 610 3.3.3), we further explore here the role of ice lenses. The ice lens density (ρ_{IL}) variations
 611 can explain part of the variability as the density of ice influences the internal reflection
 612 (Durand et al., 2008; Rutter et al., 2013). In fact, ice lenses can be snow crusts with a
 613 density as low as 630 kg m^{-3} (Marsh and Woo, 1984). However, measuring the density of
 614 such layers is challenging and it was not attempted during our campaigns. The sensitivity
 615 was evaluated for a range of ice density between 700 kg m^{-3} ($T_{B\rho_{\text{IL}700}}$) and 917 kg m^{-3}
 616 ($T_{B\rho_{\text{IL}917}}$) for all snowpits with ice lenses. The variation of T_B related to ρ_{IL} uncertainties
 617 ($\Delta T_{B\rho_{\text{IL}}} : T_{B\rho_{\text{IL}917}} - T_{B\rho_{\text{IL}700}}$) was then calculated (all other parameters being constant).

618

619 Figure 11 shows that ρ_{IL} variations have a significant impact on H-pol T_B mostly at 11
 620 and 19 GHz. The low $\Delta T_{B\rho_{\text{IL}}}$ at 37 GHz (Table 11) is not related to the insensitivity of 37
 621 GHz to ice lenses, but rather to the attenuation owing to snow grains dominating the
 622 effect of ice lenses. In fact, Table 11 shows that the effect of the variation of ice lens
 623 density decreases throughout the winter at James Bay because of increasing attenuation
 624 related to grain size metamorphism. It should be noted that no scattering occurs in these
 625 layers in the model because the R_{eff} was kept null. Hence, ρ_{IL} can only explain the
 626 underestimation of T_B , not the overestimation. Part of the error could be explained by the
 627 coherence that is not taken into account in DMRT-ML. The coherence is caused by
 628 multiple reflections within a thin layer and associated interference when the thickness of
 629 the ice lenses is less than a quarter of the wavelength ($\lambda/4$) (Mätzler et al., 1987;
 630 Montpetit et al., 2013). Since DMRT-ML does not take into account the coherence, the
 631 thickness of the ice layer has a negligible impact on T_B and was kept at 1 cm. However,
 632 simulations with MEMLS accounting for coherence have shown that variation in the ice
 633 lens thickness can change T_B by up to 100 K at H-pol at 19 and 37 GHz (Montpetit et al.,
 634 2013). Also, in this study, only the main ice lenses were noted and inserted in DMRT-
 635 ML. Many other melt/refreeze thin snow crusts were present but not recorded, and they
 636 can have a large impact on T_B observations (see Rutter et al., 2013). These thin crusts
 637 (less than 2 mm) with a high density (over 600 kg m^{-3}) can also have significant
 638 coherence effects (less than $\lambda/4$).

639

640 During the JB_{Jan} campaign, at the transect, two ice lenses were observed at three
641 consecutive snowpits (JB_{Jan} -6.7, JB_{Jan} -6.8 and JB_{Jan} -6.9). The simulations at these sites
642 show the three lowest simulated T_B at 11 GHz and 19 GHz at H-pol (Fig. 11). The second
643 observed ice lens inserted in DMRT-ML significantly decreases the simulated T_B .
644 Including the second observed ice lens allows an improvement in the T_B simulation at
645 JB_{Jan} -6.8 (Table 1), while the accuracy decreases for the two other snowpits, especially at
646 11 GHz. These results show the importance of small-scale spatial variability in the
647 distribution of ice lenses. In this case, since the SBR footprint is not exactly where the
648 snowpit was dug, the 11 GHz measured the two ice lenses at JB_{Jan} -6.8, but not at JB_{Jan} -
649 6.7 and JB_{Jan} -6.9. Rutter et al. (2013) showed that such small-scale discontinuities in ice
650 lenses have a strong impact on T_B .
651



652
653 **Fig. 11.** T_B sensitivity associated with the ρ_{IL} variation (700 to 917 $kg\ m^{-3}$).
654

655 **Table 11.** T_B sensitivity ($\Delta T_{B\rho_{IL}}$: $T_{B\rho_{IL917}} - T_{B\rho_{IL700}}$) (K) associated with the ρ_{IL} variation
656 (700 to 917 $kg\ m^{-3}$)

	JB_{Jan}	JB_{Feb}	JB_{Mar}	UMI
11H	17	15.9	11.9	13.4
11V	3.7	3.1	2.6	3.5
19H	15.4	14.3	9.2	12.1
19V	3.2	2.4	1.8	3.1
37H	6.4	5.7	1.2	6.1
37V	0.8	1.5	1.7	1.1

657

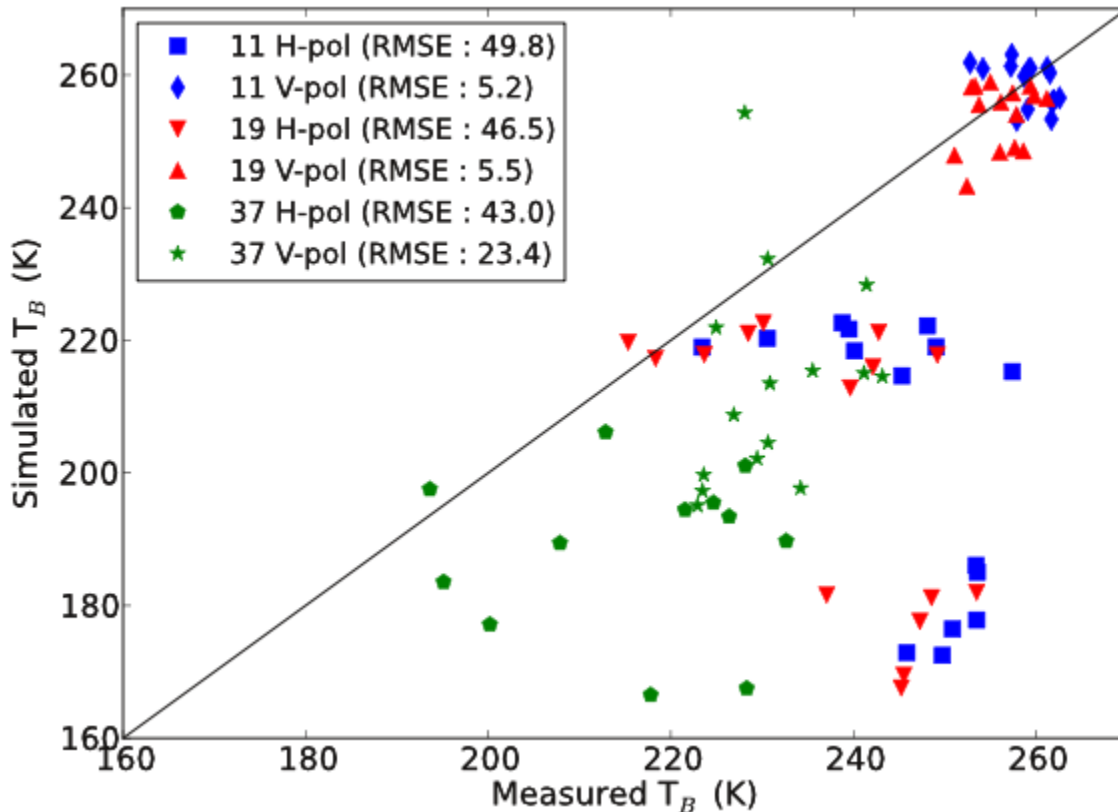
658

659 3.2.5 Surrounding vegetation effects

660

661 In a forested area, tree emission reflected by the snowpack can significantly contribute to
 662 the measured T_B on the ground (Roy et al., 2012). An analysis was conducted on 18 site
 663 measurements taken in a forest during the three James Bay campaigns (Table 4) to
 664 quantify the forest contributions to measured T_B using DMRT-ML. A first simulation,
 665 neglecting the emission coming from the trees in the downwelling T_B (T_{Bdown}) reflected
 666 by the surface was conducted. Figure 12 shows a clear underestimation (biases ≈ 40 K at
 667 H-pol) of simulated T_B at all frequencies, except for 11 and 19 GHz at V-pol. Table 12
 668 shows that these biases are much greater than the uncertainties induced by the snow cover
 669 in open areas, showing that the tree emission reflected by the surface significantly
 670 increased the measured T_B . The low influence of vegetation (low $bias_{forest}$: Table 12) at 11
 671 and 19 GHz V-pol is explained by the fact that the reflectivity of the surface at these
 672 frequencies is very low because the volume scattering is weak and the reflectivity at the
 673 interfaces is close to zero near the Brewster angle.

674



675

676 **Fig. 12.** Simulated T_B in forested sites neglecting the vegetation contribution (T_{Bdown}).

677

678 **Table 12.** Comparison between the calculated biases in an open area and in a forested
679 area

	Bias _{open}	Bias _{forest}
11H	4.7	-41.7
11V	-4.0	-1.1

19H	-4.0	-35.9
19V	-5.7	-3.4
37H	2.2	-37.4
37V	3.3	-21.4

680

681 To quantify the forest contribution, the T_{Bdown} was inverted with DMRT-ML. From the
682 simulated T_B neglecting the forest contribution (Fig. 12), an iteration process was
683 performed to find the T_{Bdown} value that minimized the $RMSE_{veg}$ between simulated and
684 measured T_B at V-pol and H-pol for each frequency independently:

685

$$686 \quad RMSE_{veg} = \sqrt{\frac{\sum_{i=1}^N (T_{Bsim;i}^{fV} - T_{Bmes;i}^{fV})^2 + (T_{Bsim;i}^{fH} - T_{Bmes;i}^{fH})^2}{2N}} \quad (6)$$

687

688 where f is the frequency.

689

690 Table 13 shows that the averaged optimized T_{Bdown} are 147 K, 120 K and 110 K
691 respectively at 11, 19 and 37 GHz. The optimized T_{Bdown} , however, decrease with
692 frequency, which is opposite to what was shown in other studies (Kruopis et al., 1999;
693 Roy et al., 2012; Roy et al., 2014). This is probably related to the inherent error in the
694 snow surface T_B simulation in DMRT-ML (Table 7), which induces error in the
695 calculation of the reflectivity of the snow-covered surface.

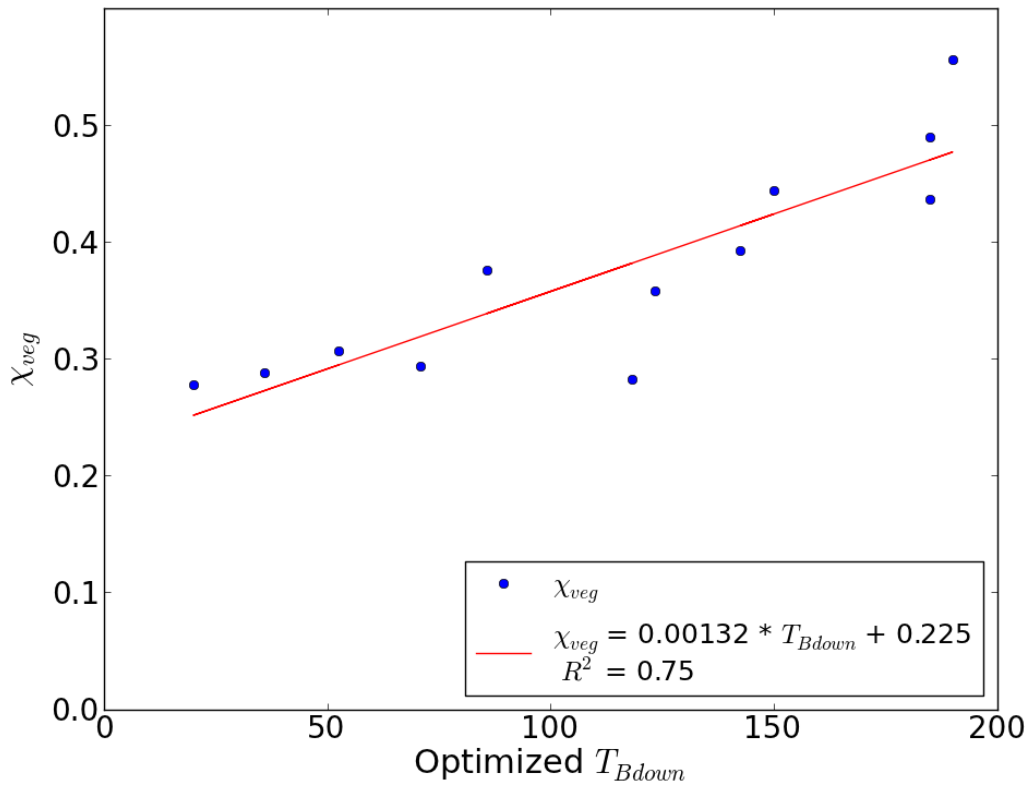
696

697 **Table 13.** Average optimized T_{Bdown} and standard deviation (in parentheses) (K)

	11 GHz	19 GHz	37 GHz
T_{Bdown} (K)	147 (± 64)	120 (± 74)	110 (± 43)

698

699 Table 13 also shows that there are large variations between the different snowpits with a
700 standard deviation between 43 K and 74 K. The average T_{Bdown} of the three frequencies
701 was calculated for each site and compared with χ_{veg} obtained from fisheye pictures taken
702 at the twelve JB_{veg} sites in January and February (fisheye pictures were not taken in
703 March). Figure 13 shows that there is a good correlation ($R^2 = 0.75$) between averaged
704 T_{Bdown} (mean for the three frequencies) and χ_{veg} . These results confirm that the optimized
705 T_{Bdown} are related to the tree emission reflected by the surface (see an example of
706 variations in Fig. 1). For comparison, the calculated atmospheric downwelling
707 contributions were around 6 K at 11 GHz and 25 K at 37 GHz. It also shows the potential
708 of using fisheye pictures to quantify tree microwave emission in boreal forests. However,
709 further considerations are necessary to improve the method. Because of the non-
710 Lambertian component of the snow reflection and the non-homogeneity of the trees
711 surrounding the site measurements, the direction (azimuth) in which the SBR is pointing
712 has an important influence on the signal (Courtemanche et al., 2015). DMRT-ML
713 assumed that the T_{Bdown} is isotropic, and does not take into account these specular
714 components. For example, the T_B will be higher if the SBR is pointing in the direction of
715 a large trunk close to the snowpit instead of pointing in the direction of a forest opening.



716 **Fig. 13.** Relationship between the average T_{Bdown} of the three frequencies and the
 717 proportion of pixels occupied by vegetation (trees) in the fisheye pictures (χ_{veg}) for the 12
 718 JB_{veg} sites in January and February.
 719

720

721 4. Discussion / conclusion

722

723 This study presents a comprehensive analysis of the geophysical factors contributing to
 724 uncertainty in DMRT-ML for snow-covered surfaces in boreal forest, subarctic and arctic
 725 environments. A unique in situ database, including key information on the snowpack
 726 temporal winter evolution, allowed the assessment of the impact of spatial variability of
 727 1) soil emission, 2) errors in snow grains and 3) density measurements, 4) ice lenses and
 728 5) vegetation emission reflected from the surface on DMRT-ML simulations.

729

730 The implementation in DMRT-ML of the bridging aiming at filling the gap between low
 731 and high snow density ranges where the theory is invalid has been tested. Bridging leads
 732 to a small improvement for tundra snow where wind slabs are present. These
 733 improvements are modest and could compensate for the measurement uncertainties or
 734 other limitations related to the use of the model such as stickiness and grain size
 735 distribution (Roy et al., 2013). Based on the work of Dierking et al. (2012), the range of
 736 the ice fraction where bridging was applied was limited to 0.4 - 0.6, but could be
 737 extended and lead to a stronger impact of bridging on the results (Tsang et al., 2008). But
 738 as shown in this study, the uncertainties in measurements make it difficult to make sure
 739 that any optimization of the bridging range does not compensate for other uncertainties.

740 In practice, this new version of DMRT-ML with bridging facilitates simulation of snow
741 and/or ice without identification of the snow layer state.

742

743 Based on several snow removal experiments, the study shows that small-scale variability
744 in soil emissivity in a boreal forest has a second order effect on the snow-covered surface
745 T_B when the soil is frozen, even for lower frequencies that are more transparent to the
746 snowpack (11 and 19 GHz). In practice, this implies that the use of constant soil
747 parameters for frozen soil emission modeling for a given environment is adequate for
748 snow emission studies. This result is surprising since soil roughness, soil wetness,
749 freeze/thaw state and stratigraphy are usually difficult to measure in boreal conditions.
750 However, further experiments should be done to validate this aspect for other types of
751 environments. Exploring larger scales could help to determine at what scale soil
752 emissivity has an influence on snow-covered T_B .

753

754 This study shows the strong sensitivity of DMRT-ML to snow grain size and density at
755 37 GHz, and that the error related to the measurements can explain most of the RMSE at
756 this frequency and probably at higher frequencies. These results are in agreement with
757 studies using MEMLS (Durand et al., 2008) and HUT (Rutter et al., 2013; Lemmetyinen
758 et al., 2015). It remains difficult to distinguish the sources of error related to DMRT-ML
759 simulations at 37 GHz. The study, however, underlines that measurement error limits the
760 accuracy of the simulations. The error related to the physical simplifications in DMRT-
761 ML was not investigated in this work, but our results suggest that the level of confidence
762 of measurements is too low to test or significantly improve the DMRT-ML physics. In
763 this study, SSA was used because it is a robust and objective metric that can be measured
764 effectively on the field. However, the derived R_{opt} metric used in DMRT-ML is related to
765 an optical definition (Grenfell and Warren, 1999) and might not represent the grain for
766 microwave wavelength (Mätzler, 2002). Further experiments on isolated snow layers as
767 done by Wiesmann et al. (1998) but using new tools for snow microstructure
768 parameterization could be applied to improve the physics of emission models. For
769 example, more precise measurements of snow microstructure like X-ray tomography
770 (Heggli et al., 2011) and the snow micro-penetrometer (SMP) (Schneebeli et al., 1999;
771 Proksch et al., 2015) could be the next step to improve the understanding of the physics
772 in DMRT-ML (e.g., Lowe and Picard, 2015). However, each snow microstructure
773 measurement method has its own limitations. Combining the different information could
774 be an avenue to better quantify the snow scattering mechanism in DMRT-ML.

775 This analysis confirms that the scaling factor ($\phi = 3.3$) proposed by Roy et al. (2013) is a
776 general value as it yields accurate results with the new data set presented in this paper.
777 We do not pretend that this value exactly applies to other environments as Picard et al.
778 (2014) found a lower value (2.3) for Antarctica with a SSA measurement technique that
779 was inter-calibrated with ours. The temporal analysis during the three campaigns in
780 James Bay, however, shows that the sensitivity to snow measurement uncertainties
781 evolve during winter due to snow metamorphism. This sensitivity change is also
782 important at 19 GHz. Although snow is almost transparent at this frequency at the
783 beginning of winter when the grains are small, T_B at 19 GHz becomes sensitive to snow
784 in March because of snow grain growth. This could be of interest for the SWE retrieval
785 approach, knowing that 19 GHz T_B becomes sensitive to snow when snow grains become

786 larger. As proposed in Derksen (2008) 11 and 19 GHz frequencies could be useful for
787 SWE retrievals for deep snow to overcome the problem of saturation at 37 GHz (see
788 Rosenfeld and Grody, 2000). At 11 GHz, snow is almost transparent throughout the
789 winter demonstrating the utility of this band for monitoring soil conditions (phase,
790 temperature) under the snow (Kohn and Royer, 2010).

791

792 The inclusion of ice lenses in DMRT-ML significantly improves the simulations at H-
793 pol. However, the model is not able to reproduce the observed spatial variability at 11
794 and 19 GHz at H-pol, which was shown to be related to snowpack stratigraphy
795 inaccuracies, mostly related to ice lenses and strong variations in snow density (for
796 example, thin snow crust). The large spatial variability of ice lenses and snow crusts at
797 the meter scale (Rutter et al., 2013) can lead to the strong spatial variability of observed
798 T_B . This ice lenses and snow crust spatial variability raise the need to develop efficient
799 and practical methods to effectively characterize ice lenses and thin snow crusts,
800 especially their density (Marsh and Woo, 1984). Using short-wave infrared photography
801 (Montpetit et al., 2012) or SMP profiles (Proksch et al., 2015) are possible options. The
802 coherence, which is not taken into account in DMRT-ML, is responsible for a large
803 sensitivity of T_B to ice lens thickness and can explain the observed T_B variability at 19
804 and 11 GHz at H-pol. The implementation of the coherence in DMRT-ML is not difficult,
805 but collecting the input variables in the field remains the major challenge.

806

807 In boreal forest areas, our analysis shows that the vegetation emission reflected by the
808 snow-covered surface can contribute more than 200 K and that neglecting the reflection
809 of the signal on the snow surface can lead to a bias of up to 40 K, mostly at H-pol where
810 the surface reflectivity is the highest. This bias is coupled to the snow state, depending on
811 the snow reflectivity. These results clearly show the importance of the vegetation
812 contribution and avoiding this contribution in measurements imply to operate in clearings
813 with minimal forest cover mostly on the opposite side of the measurements (specular
814 contributions). However, some promising results on the use of fisheye photographs to
815 quantify that vegetation contribution were shown. The use of a Lambertian microwave
816 surface for retrieving the downwelling contribution in ground-based radiometric
817 measurements (Courtemanche et al., 2015) may also be a promising avenue.

818

819 To the best of our knowledge, this is the first time that an analysis has been carried out of
820 all the elements (soil, grain size, snow density, ice lenses, and vegetation) that contribute
821 to the microwave signal at three frequencies (36.5, 18.7 and 10.65 GHz) in a boreal
822 forest. The study sheds light on DMRT-ML uncertainties related to small-scale variability
823 and measurement errors in different environments and for different periods in the winter.
824 Some limitations were raised on the accuracy of DMRT-ML to simulate the T_B of snow-
825 covered surfaces, and this analysis will help to design future studies to improve the
826 ability of DMRT-ML and other MESM to model the radiative transfer processes of snow-
827 covered surfaces.

828

829

830 *Acknowledgements*

831

832 The authors would like to thank the National Sciences and Engineering Research Council
833 of Canada (NSERC) and Environment Canada for their financial support. The French
834 collaboration was supported by the Programme de développement de partenariats
835 stratégiques en matière d'enseignement et de recherche (FRQNT- Conseil franco-
836 québécois de la coopération universitaire); Patrick Cliche, Serge Langlois, Nathalie
837 Thériault, Caroline Dolant and Bruno-Charles Busseau (Université de Sherbrooke), Éric
838 Lefebvre (Laboratoire de glaciologie et géophysique de l'environnement de Grenoble),
839 Bernard Lesaffre (CNRM-GAME, MétéoFrance-CNRS) and Florent Dominé and
840 Mathieu Barrère (Takuvik and Université Laval) for their contributions to the field work
841 to obtain these measurements; Peter Toose and Chris Derksen (Environment Canada) for
842 providing part of Churchill data. The French polar institute (IPEV) has contributed
843 through the BIPOL project. We also thank Élie Girard, Université de Sherbrooke, for his
844 contributions in data processing and simulations. We would like to thanks the two
845 anonymous reviewers for their helpful comments.

846

847

848 **References**

849

850 Armstrong, R. L., and Brun, E.: *Snow and Climate: Physical Processes, Surface Energy*
851 *Exchange and Modeling*, Cambridge University Press, 222 pp., 2008.

852

853 Brucker, L., Picard, G., Arnaud, L., Barnola, J.-M., Schneebeli, M., Brunjail, H.,
854 Lefebvre, E., and Fily, M.: Modelling time series of microwave brightness temperature at
855 Dome C, Antarctica, using vertically resolved snow temperature and microstructure
856 measurements, *J. Glaciol.*, 57, 171–182, 2011.

857

858 Champollion, N., Picard, G., Arnaud, L., Lefebvre, E., and Fily, M.: Hoar crystal
859 development and disappearance at Dome C, Antarctica: observation by near-infrared
860 photography and passive microwave satellite, *The Cryosphere*, 7, 1247–1262,
861 doi:10.5194/tc-7-1247-2013, 2013.

862

863 Chang, A. T. C., Foster, J. L., and Hall, D. K.: Nimbus-7 SMMR derived
864 global snow cover parameters, *Ann. Glaciol.*, 9, 39–44, 1987.

865

866 Colbeck, S.: Theory of metamorphism of dry snow, *J. Geophys. Res.*, 88, 5475–5482,
867 1983.

868

869 Courtemanche, B., Montpetit, B., Royer, A., and Roy, A.: Creation of a Lambertian
870 microwave surface for retrieving the downwelling contribution in ground-based
871 radiometric measurements, *IEEE T. Geosci. Remote*, 12, 462–466, 2015.

872

873 Derksen, C.: The contribution of AMSR-E 18.7 and 10.7 GHz measurements to improved
874 boreal forest snow water equivalent retrievals, *Remote Sens. Environ.*, 112, 2701–2710,
875 2008.

876

877 Derksen, C., Toose, P., Lemmetyinen, J., Pulliainen, J., Langlois, A., Rutter, N., and
878 Fuller, M.: Evaluation of passive microwave brightness temperature simulations and

879 snow water equivalent retrievals through a winter season, *Remote Sens. Environ.*, 117,
880 236–248, 2012.

881

882 Déry, S. J., Hernandez-Henriquez, M. A., Burford, J. E., and Wood, E. F.: Observational
883 evidence of an intensifying hydrological cycle in the northern Canada, *Geophys. Res.*
884 *Lett.*, 36, L13402, 2009.

885

886 Dierking, W., Linow, S., and Rack, W.: Toward a robust retrieval of snow accumulation
887 over the Antarctic ice sheet using satellite radar, *J. Geophys. Res.*, 117, D09110,
888 doi:10.1029/2011JD017227, 2012

889

890 Dupont, F., Picard, G., Royer, A., Fily, M., Roy, A., Langlois, A., and Champollion, N.:
891 Modeling the microwave emission of bubbly ice: applications to blue ice and
892 superimposed ice in the Antarctic and Arctic, *IEEE T. Geosci. Remote*, 52, 6639–6651,
893 2014.

894

895 Durand, M., Kim, E. C., and Margulis, S.: Quantifying uncertainty in modeling snow
896 microwave radiance for a mountain snowpack at the point-scale, including stratigraphic
897 effects, *IEEE T. Geosci. Remote*, 46, 1753–1767, 2008.

898

899 Gallet, J.-C., Domine, F., Zender, C. S., and Picard, G.: Measurement of the specific
900 surface area of snow using infrared reflectance in an integrating sphere at 1310 and 1550
901 nm, *The Cryosphere*, 3, 167–182, doi:10.5194/tc-3-167-2009, 2009.

902

903 Goodison, B., Rubinstein, I., Thirkettle, F., Langham, E.: Determination of snow water
904 equivalent on the Canadian Prairies using microwave radiometry, *Proc. of the Budapest*
905 *Symposium*, 163–173, 1986.

906

907 Gouttevin, I., Menegoz, M., Dominé, F., Krinner, G., Koven, C., and Ciais, P.: How the
908 insulating properties of snow affect soil carbon distribution in the continental pan-Arctic
909 area, *J. Geophys. Res.*, 117, G02020, 2012.

910

911 Grenfell, T. C., and Warren, S. G.: Representation of a nonspherical ice particle by
912 collection of independent spheres for scattering and absorption of radiation, *J. Geophys.*
913 *Res.*, 104, 31697-31709, 1999.

914 

915 Latifovic, R., Zhu, Z.-L., Cihlar, J., Giri, C., and Olthof, I.: Land cover mapping of North
916 and Central America – Global land cover 2000. *Remote Sens. Environ.*, 89, 116–127,
917 2004.

918

919 Liston, G. E., McFadden, J. P., Sturm, M., and Pielke, R. A.: Modelled changes in arctic
920 tundra snow, energy and moisture fluxes due to increased shrubs, *Glob. Change Biol.*, 8,
921 17–32, 2002.

922

923 Heggli, M., Köchle, B., Matzl, M., Pinzer, B.R., Riche, F., Steiner, S., Steinfeld, D.,
924 and Schneebeli, M.: Measuring snow in 3-D using X-ray tomography: assessment of
925 visualization techniques, *Ann. Glaciol.*, 52, 231–236, 2011.

926

927 Jin, Y.: *Electromagnetic Scattering Modelling for Quantitative Remote Sensing*.
928 Singapore: World Scientific, 1994.

929

930 Kokhanovsky, A. A. and Zege, E. P.: Scattering optics of snow, *Appl. Optics*, 43, 1589–
931 1602, 2004.

932

933 Kohn, J., and Royer, A.: AMSR-E data inversion for soil temperature estimation under
934 snow cover, *Remote Sens. Environ.*, 114, 2951–2961, 2010.

935

936 Kontu, A. and Pulliainen, J.: Simulation of spaceborne microwave radiometer
937 measurements of snow cover using in situ data and brightness temperature modeling,
938 *IEEE T. Geosci. Remote*, 48, 1031–1044, 2010.

939

940 Kruopis, N., Praks, J., Arslan, A. N., Alasalmi, H. M., Koskinen, J. T., and Hallikainen,
941 M. T.: Passive microwave measurements of snow-covered forest area in EMAC'95. *IEEE*
942 *T. Geosci. Remote*, 37, 2699–2705, 1999.

943

944 Langlois, A.: Applications of the PR series radiometers for cryospheric and soil moisture
945 research, Radiometrics Corporation, 40 pp., 2015.

946

947 Larue, A., Royer, A., De Sève, D., Langlois, A., and Roy, A.: Validation analysis of the
948 GlobSnow2 database over an eco-climatic latitudinal gradient in Eastern Canada, *J.*
949 *Hydrometeorol.*, in redaction, 2015.

950

951 Lemmetyinen, J., Pulliainen, J., Rees, A., Kontu, A., Qiu, Y., and Derksen, C.: Multiple-
952 layer adaptation of HUT snow emission model: Comparison with experimental data,
953 *IEEE T. Geosci. Remote*, 48, 2781–2794, 2010.

954

955 Lemmetyinen, J., Derksen, C., Toose, P., Proksh, M., Pulliainen, J., Kontu, A.,
956 Rautiainen, K., Seppänen, J., Hallikainen, M.: Simulating seasonally and spatially varying
957 snow cover brightness temperature using HUT snow emission model and retrieval of a
958 microwave effective grain size, *Remote Sens. Environ.*, 156, 71–95, 2015.

959

960 Lemmetyinen, J., Schwank, M., Rautiainen, K., Kontu, A., Parkkinen, T., Mätzler, C.,
961 Wiesmann, A., Wegmüller, U., Derksen, C., Toose, P., Roy, A., and Pulliainen, J.: Snow
962 density and ground permittivity retrieved from L-Band radiometry: application to
963 experimental data, *Remote Sens. Environ.*, In review, 2015.

964

965 Liebe, H.: MPM—An atmospheric millimeter-wave propagation model, *Int. J. Infrared*
966 *Millim. Waves*, 10, 631–650, 1989.

967

968 Löwe, H. and Picard, G.: Microwave scattering coefficient of snow in MEMLS and

969 DMRT-ML revisited: the relevance of sticky hard spheres and tomography-based
970 estimates of stickiness, *The Cryosphere Discuss.*, 9, 2495–2542, doi:10.5194/tcd-9-2495-
971 2015, 2015.

972

973 Marsh, P., and Woo, M.-K.: Wetting front advance and freezing of meltwater within a
974 snow cover 1. Observations in the Canadian arctic, *Water Resour. Res.*, 20, 1853–1864,
975 1984.

976

977 Mätzler, C.: Relation between grain-size and correlation length of snow, *J. Glaciol.*, 48,
978 461-466, 2002.

979

980 Mätzler, C.: Applications of the interaction of microwaves with natural snow cover,
981 *Remote Sens. Rev.*, 2, 259-392, 1987.

982

983 Mesinger, F., Dimego, G., Kalnay, E., Mitchell, K., Shafran, P. C., Ebisuzaki, W., Jovic,
984 D., Woollen, J., Rogers, E., Berbery, E. H., Ek, M. B., Fan, Y., Grumbine, R., Higgins,
985 W., Li, H., Lin, Y., Manikin, G., Parrish, D. and Shi, W.: North American regional
986 reanalysis, *Bull. Amer. Meteorol. Soc.*, 87, 343–360, 2006.

987

988 Montpetit, B., Royer, A., Langlois, A., Cliche, P., Roy, A., Champollion, N., Picard, G.,
989 Domine, F., and Obbard, R.: New shortwave infrared albedo measurements for snow
990 specific surface area retrieval, *J. Glaciol.*, 58, 941,
991 doi:10.1016/j.coldregions.2010.01.004, 2012.

992

993 Montpetit, B., Royer, A., Roy, A., Langlois, L., and Derksen, C.: Snow microwave
994 emission modeling of ice lenses within a snowpack using the microwave emission model
995 for layered snowpacks, *IEEE T. Geosci. Remote*, 51, 4705–4717,
996 doi:10.1109/TGRS.2013.2250509, 2013.

997

998 Montpetit, B.: Analyse de la modélisation de l'émission multi-fréquences micro-ondes et
999 de la neige, incluant les croutes de glace à l'aide du modèle Microwave Emission Model
1000 of Layered Snowpack (MEMLS), Ph.D thesis, Université de Sherbrooke, 168 pp,
1001 <http://hdl.handle.net/11143/6844>.

1002

1003 Picard, G., Brucker, L., Roy, A., Dupont, F., Fily, M., and Royer, A.: Simulation of the
1004 microwave emission of multi-layered snowpacks using the dense media radiative transfer
1005 theory: the DMRT-ML model, *Geosci. Model Dev. Discuss.*, 5, 3647–3694,
1006 doi:10.5194/gmdd-5-3647-2012, 2012.

1007

1008 Picard, G., Royer, A., Arnaud, L., and Fily, M.: Influence of meter-scale wind-formed
1009 features on the variability of the microwave brightness temperature around Dome C in
1010 Antarctica, *The Cryosphere*, 8, 1105-1119, doi:10.5194/tc-8-1105-2014, 2014.

1011

1012 Proksch, M., Löwe, H., and Schneebeli, M: Density, specific surface area, and correlation
1013 length of snow measured by high-resolution penetrometry, *J. Geophys. Res. Earth Surf.*,
1014 120, 346–362, doi:10.1002/2014JF003266, 2015.

1015
1016 Rees, A., Lemmetyinen, J., Derksen, C., Pulliainen, J. T., and English, M.: Observed and
1017 modelled effects of ice lens formation on passive microwave brightness temperatures
1018 over snow covered tundra, *Remote Sens. Environ.*, 114, 116–126, 2010.
1019
1020 Rosenfeld, S., and Grody, N.: Anomalous microwave spectra of snow cover observed
1021 from Special Sensor Microwave/Imager measurements, *J. Geophys. Res.*, 105, D11,
1022 14913–14925, 2000.
1023
1024 Roy, A., Royer, A., and Turcotte, R.: Improvement of springtime streamflow simulations
1025 in a boreal environment by incorporating snow-covered area derived from remote sensing
1026 data, *J. Hydrol.*, 390, 35–44, 2010.
1027
1028 Roy, A., Royer, A., Wigneron, J.-P., Langlois, A., Bergeron, J., and Cliche, P.: A simple
1029 parameterization for a boreal forest radiative transfer model at microwave frequencies,
1030 *Remote Sens. Environ.*, 124, 371–383, 2012.
1031
1032 Roy, A., Picard, G., Royer, A., Montpetit, B., Dupont, F., Langlois, A., Derksen, C., and
1033 Champollion, N.: Brightness temperature simulations of the Canadian seasonal snowpack
1034 driven by measurements of the snow specific surface area, *IEEE T. Geosci. Remote*, 51,
1035 4692–4704, doi:10.1109/TGRS.2012.2235842, 2013.
1036
1037 Roy, A., Royer, A., and Hall, J. R.: Relationship between forest microwave
1038 transmissivity and structural parameters for the Canadian boreal forest, *Geophys. Res.*
1039 *Lett.*, 11, 1802–1806, 2014.
1040
1041 Roy, A., Royer, A., Montpetit, B., and Langlois, A.: Microwave snow emission modeling
1042 of boreal forest environments, *Proc. IGARSS2015*, Milan, Italy, July, 754-757, 2015.
1043
1044 Rutter, N., Sandells, M., Derksen, C., Toose, P., Royer, A., Montpetit, B., Langlois, A.,
1045 Lemmetyinen, J., and Pulliainen, J.: Snow stratigraphic heterogeneity within ground-
1046 based passive microwave radiometer footprints: Implications for emission modeling, *J.*
1047 *Geophys. Res. Earth Surf.*, 119, 550–565, doi:10.1002/2013JF003017, 2013.
1048
1049 Schneebeli, M., Pielmeier, C., and Johnson, J.: Measuring snow microstructure and
1050 hardness using a high resolution penetrometer, *Cold Reg. Sci. Technol.*, 30, 101–114,
1051 doi:10.1016/S0165-232X(99)00030-0, 1999.
1052
1053 Schuur, E. A. G., Abbott, B.W., Bowden, W.B., Brovkin, V., Camill, P., and Canadell,
1054 J.G.: Expert assessment of vulnerability of permafrost carbon to climate change. *Clim.*
1055 *Change*, 119, 359–374, 2013.
1056
1057 Takala, M., Luojus, K., Pulliainen, J., Derksen, C., Lemmetyinen, J., Kärnä, J.-P., and
1058 Koskinen, J.: Estimating northern hemisphere snow water equivalent for climate research
1059 through assimilation of space-borne radiometer data and ground-based measurements,
1060 *Remote Sens. Environ.*, 115, 3517–3529, 2011.
1061

1062 Tedesco, M., and Kim, E. J.: Intercomparison of electromagnetic models for passive
1063 microwave remote sensing of snow, *IEEE T. Geosci. Remote*, 44, 2654–2666, 2006.
1064
1065 Tsang, L., Kong, J. A., Ding, K.-H., and Ao C. O.: *Scattering of Electromagnetic Waves:
1066 Numerical Simulations*. New York, NY, USA: Wiley, 2001.
1067
1068 Tsang, L., Liang, D., Xu, X., and Xu, P.: Microwave emission from snowpacks:
1069 Modeling the effects of volume scattering, surface scattering and layering, in *Proc. 10th
1070 Spec. Meet. Microw. Radiometry Remote Sens. Environ. (MicroRad)*, Firenze, Italy,
1071 Mar. 11–14, pp.1–4, 2008.
1072
1073 Wegmüller, U., and Mätzler, C.: Rough bare soil reflectivity model, *IEEE T. Geosci.
1074 Remote.*, 37, 1391–1395, 1999.
1075
1076 Wiesmann, A., Mätzler, C., and Weise, T.: Radiometric and structural measurements of
1077 snow samples, *Radio Sci.*, 33, 273–289, 1998.
1078